Late orogenic exhumation of the Variscan high-grade units (South Armorican Domain, western France), combined structural and 40Ar/39Ar constraints

Paul Turrillot, Romain Augier, Patrick Monié, Michel Faure

Late orogenic exhumation of the Variscan high-grade units (South Armorican Domain, western France), combined structural and ^{40}Ar/^{39}Ar constraints

Paul Turrillot,[1,2] Romain Augier,[1] Patrick Monié,[3] and Michel Faure[1]

[1]   The current structure of the South Armorican Domain in the French Variscan Belt, provides an excellent record of the late orogenic evolution, as documented by the complex interactions between extensional structures and partial melting. In the Golfe du Morbihan, the South Brittany Migmatite Belt (SBMB), tectonically overlain by non-melted metamorphic units, was studied by combined structural and ^{40}Ar/^{39}Ar methods. The recognition of successive deformation stages points to a strain continuum initiated at depth at the end of a partial melting event, and continued to near-surface brittle faulting, encompassing ductile strain localization over a major top-to-the-ESE extensional shear zone (SSZ) consistent with an overall WNW-ESE orogen-parallel stretching. This multidisciplinary study making the link between structure, texture, microchemistry and ^{40}Ar/^{39}Ar geochronology allow distinguishing between cooling, recrystallization and syn-tectonic crystallization ages. The first extensional insights, witnessed by dyke intrusion were dated at ~319 ± 6 Ma immediately after the SBMB partial melting. Strain localization along the SSZ, occurred until ~302–298 Ma when SBMB crossed the ductile-brittle transition. Moreover, in situ ^{40}Ar/^{39}Ar analysis, of syn-tectonic white micas sampled in the ductile and brittle structures yield similar ~300 Ma. Formation or reactivation of the SSZ may have occurred during the rapid cooling of the SBMB settled at ~305 Ma by conventional ^{40}Ar/^{39}Ar analysis. Large-scale late orogenic extensional event of the previously overthickened Variscan crust thus lasted over ~20 ± 3 Myr in the same extensional tectonic regime guided by the South Armorican Shear Zone.

1. Introduction

[2] In convergent tectonic settings, while rock burial is mostly understood, mechanisms and processes by which deep-seated metamorphic rocks of highly extended areas were transported back to the surface are still debated [e.g., *Wernicke*, 1992; *Axen et al.*, 1998; *Jolivet et al.*, 2003]. Syn-orogenic exhumation during subduction and collision, often attested by the preservation of high-pressure-low-temperature (HP-LT) metamorphic assemblages [e.g., *Platt*, 1986; *Agard et al.*, 2005] is completed by late orogenic processes. Questions on the mechanisms allowing the re-equilibration of the crust in such late orogenic context are still discussed

[e.g., *Rey et al.*, 2001, 2009; *Tirel et al.*, 2008]. The lower parts of mature orogens commonly contains a series of gneiss domes composed of high-grade metamorphic rocks affected by widespread partial melting [e.g., *Teyssier and Whitney*, 2002; *Brown*, 2005]. Gneiss domes, and particularly metamorphic core complexes strengthen the link between post-collisional decompression and widespread crustal anatexis responsible for the upward mass transfer of lower-to-middle crust as an efficient mechanism for heat advection and overall cooling [*Teyssier and Whitney*, 2002; *Brown*, 2005]. Metamorphic core complexes result from a strong tectonic denudation in a continental lithospheric extension context and lead to consider a large amount of extension. While a close relationship between the presence of melts and deformation is often observed, the genetic relationships between partial melting and strain localization is still debated [e.g., *Wernicke*, 1981, 1992; *Lister et al.*, 1984; *Malavieille*, 1993; *Brown and Rushmer*, 1997; *Andersen*, 1998; *Labrousse et al.*, 2002; *Vanderhaeghe*, 2004; *Jolivet et al.*, 2005; *Charles et al.*, 2011]. Crustal melting reduces the strength of the bulk lithosphere, favoring deformation [e.g., *Van der Molen and Paterson*, 1979; *Davy et al.*,

[1]Institut des Sciences de la Terre d'Orléans, Université d'Orléans–CNRS UMR 6113–Université François Rabelais–Tours–INSU, Orléans, France.
[2]BRGM-GEO/G2R, Orléans, France.
[3]UMR 5243, Université de Montpellier 2, CNRS, Montpellier, France.

1995; *Ranalli*, 1997, 2003; *Handy and Brun*, 2004] an ultimately orogenic collapse [e.g., *Hollister*, 1993; *Faure et al.*, 1999; *Jolivet et al.*, 2005]. Furthermore, decompression during exhumation of high-grade rocks drives partial melting leading to the development of a positive feedback between partial melting and decompression [*Vanderhaeghe and Teyssier*, 2001; *Teyssier and Whitney*, 2002]. In parallel, large-scale detachment shear zones play a major role in the exhumation of metamorphic rocks. Thus, the interactions between crustal anatexis, melt extraction, and ductile and brittle deformations at the scale of an orogen need to be better understood. In addition, if the overall structure and the kinematics of the main shear zones are often well documented, precise estimations for bulk deformation duration has been proven difficult in the past and is now partially circumvented using in situ dating of syn-tectonic minerals [e.g., *Müller*, 2003; *Agard et al.*, 2002; *Maurel et al.*, 2003; *Mulch and Cosca*, 2004; *Augier et al.*, 2005a]. It is therefore of prime importance to derive precisely the duration of deformation and establish the rates at which strain is accommodated in mylonitic shear zones [*Müller*, 2003; *Mulch and Cosca*, 2004]. Major shear zone (i.e., crustal-scale) formation is a consequence of peculiar crust behavior leading to intense strain localization [*Buck*, 1991; *Corti et al.*, 2003] which increases toward ductile-brittle conditions. Conversely, strain may also accumulate pervasively prior to shear zone formation [*Tirel et al.*, 2008]. Recognition of the full succession of deformation stages of a single tectonic event, development of accurate geochronological tools, and original dating strategies then appear as new frontiers in the field of geodynamics, particularly for pre-mylonitic and post-mylonitic brittle stages.

[3] In the French Variscan Belt, the South Armorican Domain provides a good example of late orogenic gravitational collapse [*Gapais et al.*, 1993; *Brown*, 2005]. The overall framework of the internal zones displays a series of structural culminations of exhumed middle-to-lower-crustal domains made of high-grade rocks (i.e., migmatites and residual granulites) pertaining to the South Brittany Migmatite Belt (SBMB) [*Brown*, 2005], roofed, or not, by extensional shear zones [*Cagnard et al.*, 2004; *Augier et al.*, 2011]. The present study focuses on the Golfe du Morbihan and western neighboring areas where the late orogenic events are particularly well expressed and characterized by the most important extensional shear zones of the French Armorican Massif. In order to unravel the kinematics and constrain the complete exhumation history of the deepest tectonic unit of the Variscan orogenic system in the Armorican Massif, a detailed structural study was performed on the most complete succession of extensional deformational stages, from ductile to brittle conditions, developed within the SBMB. Furthermore, combined conventional and in situ $^{40}Ar/^{39}Ar$ analyses have been undertaken on successive mineral generations whose syn-tectonic character, with respect to the deformational stages, has been recognized. Absolute ages attributed to the main stages are then discussed in terms of the most probable significance of the ages and duration of the whole late orogenic evolution of the Variscan Belt (i.e., thermochronology versus crystallization

ages). Implications of the exhumation of the SBMB for the regional tectonics are also discussed.

2. Geological Setting

2.1. The South Armorican Domain

[4] The French Massif Armorican forms the northern branch of the Ibero-Armorican orocline of the Variscan Belt of Western Europe [*Matte*, 2001]. The structural grain of this large massif is dominated by W-E to NW-SE striking dextral strike-slip faults active in the Carboniferous times, namely the North Armorican Shear Zone (NASZ), and the South Armorican Shear Zone (SASZ), in the northern and southern parts of the massif, respectively [e.g., *Cogné*, 1974; *Watts and Williams*, 1979; *Jégouzo*, 1980; *Matte*, 1986; *Le Corre et al.*, 1991] (Figure 1a).

[5] Between the northern and the southern branches of the SASZ, the Ligerian Domain is a segment of the Early Paleozoic Variscan suture zone marked by ophiolites, eclogites and high pressure gneiss, and Devonian migmatites exposed south of the Nort-sur-Erdre Fault Zone [*Marchand*, 1981; *Ballèvre et al.*, 1994; *Bosse et al.*, 2000; *Cocherie et al.*, 2005] (Figure 1a).

[6] To the South of the southern branch of the SASZ, the South Armorican Domain exhibits the most metamorphosed units of the Massif Armorican [*Berthé et al.*, 1979; *Jégouzo*, 1980].

[7] Only the geology of the South Armorican Domain is detailed below and the readers unfamiliar with the geology of the French Massif Armorican are referred to recent publications [*Gumiaux et al.*, 2004; *Faure et al.*, 2005, 2008; *Ballèvre et al.*, 2009].

[8] Regionally, in the South Armorican Domain, the following units can be described from top to bottom [e.g., *Cogné*, 1949, 1974; *Le Corre et al.*, 1991]:

[9] 1. The Upper units are characterized by HP–LT metamorphic rocks belonging to two distinctive groups. The uppermost ones (Bois de Céné and Ile de Groix klippes) are made of lawsonite-glaucophane blueschists, garnet blueschists and eclogites derived from metabasites and metasediments [*Bosse et al.*, 2000]. P-T estimates reveal that metamorphic peak conditions reached around 14–19 kbar, and 500–550°C and were followed by a limited retrogression into the greenschist-facies [*Bosse et al.*, 2002].

[10] 2. The Intermediate units correspond to the Vilaine and Belle Ile groups, are made of metavolcanics and inter-layered dark schists and black shales. Recent P-T estimates for the Belle Ile group yielded MP/LT metamorphic peak conditions of 7–9 kbar and 350–400°C [*Le Hébel et al.*, 2002b]. The Vilaine group mainly consists of micaschists equilibrated under a MP-MT gradient. Metamorphism increases downward from albite greenschist-facies to garnet-staurolite-biotite amphibolite-facies conditions [*Triboulet and Audren*, 1988; *Goujou*, 1992; *Brown and Dallmeyer*, 1996]. In the Vilaine Estuary area, metamorphic peak conditions estimates yielded 7–9 kbar for 600–650°C [*Triboulet and Audren*, 1985, 1988; *Brown and Dallmeyer*, 1996].

[11] 3. The Lower unit consists of migmatites and anatectic granitoids both belonging to the SBMB and intruded by large volumes of granites [e.g., *Audren and Le Métour*, 1976; *Marchildon and Brown*, 2003]. P-T estimates of
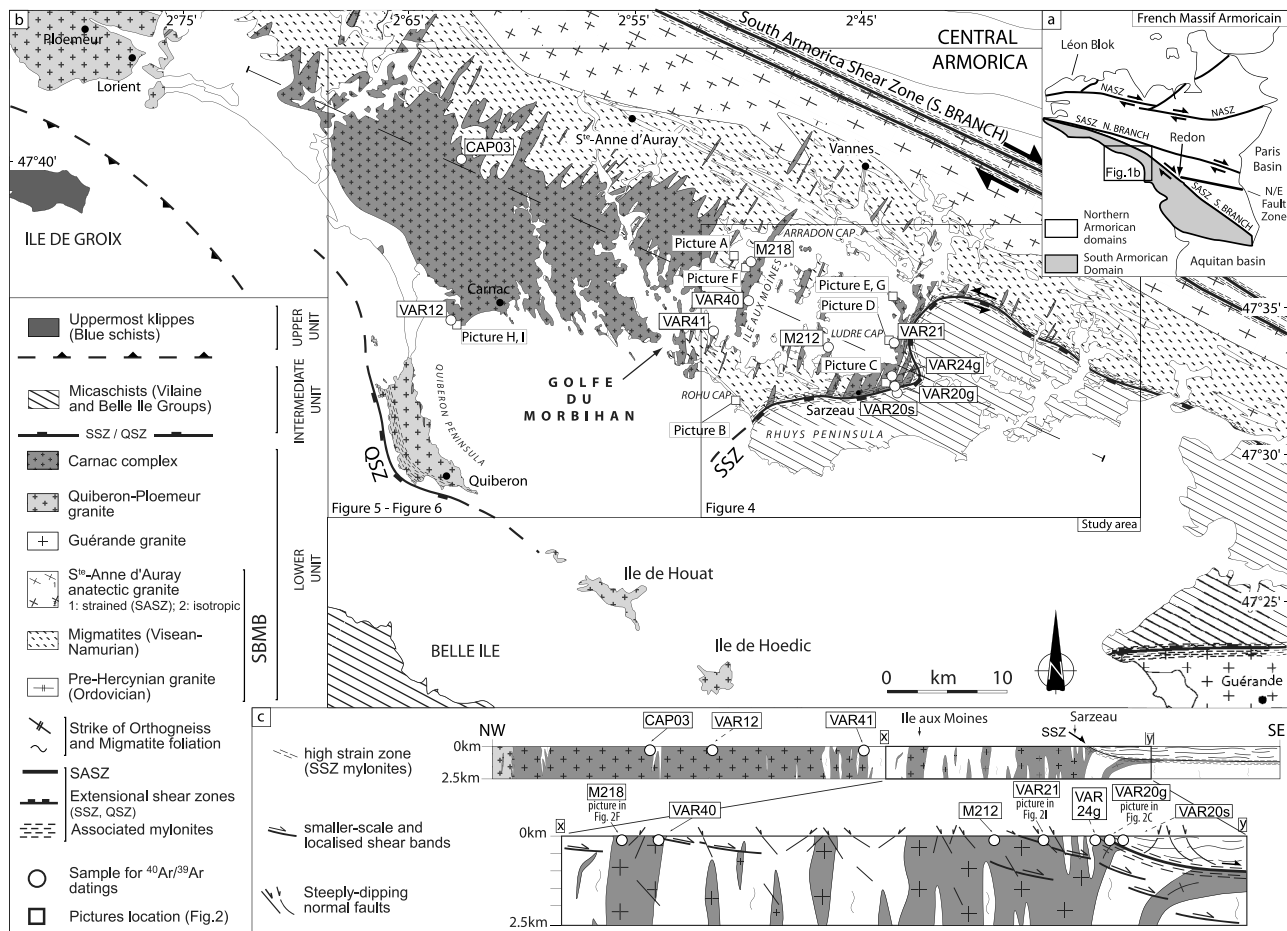
Figure 1. Geological map of the study area and location of the samples used for the ^{40}Ar/^{39}Ar analyses. (a) Simplified geological map of the French Massif Armorican showing the main tectonics domains of the massif. NASZ: North Armorican Shear Zone; SASZ: South Armorican Shear Zone; N. Branch: Northern Branch; S. Branch: Southern Branch; N/E: Nort-sur-Erdre fault. (b) Detailed map of the studied part of the South Armorican Domain, in the Golfe du Morbihan area. This geological map exhibits the main tectonometamorphic units and their overall internal features. SBMB: South Brittany Migmatite Belt. Geology of Central Armorican domain, north of SASZ is not detailed. South of the SASZ, the Upper Unit cropping out in the Ile de Groix klippe, the Intermediate and the Lower tectonic units are shown. These two latter units are separated by late orogenic extensional shear zones: the Sarzeau Shear Zone (SSZ) in the Rhuys peninsula area and the Quiberon Shear Zone (QSZ) in the Quiberon peninsula area. White squares locate hand-sample and outcrops pictures displayed on Figure 2. White circles locate samples used for the conventional and in situ ^{40}Ar/^{39}Ar analyses. Legend for the main geological formations is the same for the map and for the cross sections. (c) Interpretative cross section (dashed line on Figure 1b) through the study area. The structural features of the Golfe du Morbihan-Rhuys peninsula section (noted X-Y) have been detailed. This close-up view shows the different ductile, ductile-brittle and brittle structures described during the structural analysis. Pictures of such structures are reported in Figure 2. Location of samples used for ^{40}Ar/^{39}Ar analyses has been projected onto the cross sections.

metamorphic peak conditions yielded 8–10 kbar and 750–800°C [*Brown*, 1983; *Jones and Brown*, 1989, 1990; *Brown and Dallmeyer*, 1996; *Marchildon and Brown*, 2003; *Johnson and Brown*, 2004].

[12] Despite recent geochronological studies, the time-constrained tectonic evolution of the South Armorican Domain remains widely incomplete. However, an overall two-stepped tectonometamorphic evolution of the domain can be drawn. Metamorphic phengites from HP assemblages of the Upper HP-LT units yielded Late Devonian-Early Carboniferous ^{40}Ar/^{39}Ar ages at 370–360 Ma, while retro-

gression and final cooling (i.e., partial greenschist-facies recrystallization) occurred at around 350 Ma [*Bosse et al.*, 2000; *Le Hébel*, 2002]. These rather early ages are interpreted in terms of syn-orogenic exhumation, because most of these units were emplaced by thrusting [*Iglesias and Brun*, 1976; *Vauchez et al.*, 1987; *Goujou*, 1992; *Bosse et al.*, 2002; *Faure et al.*, 2008]. The kinematics of thrusting and its consistency at a regional scale are currently not documented [*Le Hébel*, 2002]. Subsequently, the South Armorican Domain underwent a widespread post-thickening extension as documented by detachment zones formation and metamorphic

core complexes exhumation [*Gapais et al.*, 1993; *Brown*, 2005; *Turrillot et al.*, 2009]. The overall framework of the South Armorican Domain consists in tectonic windows of the Lower Unit surrounded by the overlying Intermediate and Upper units characterized by a regional flat-lying planar fabric, and a dominantly W-E to NW-SE stretching lineation [*Gapais et al.*, 1993; *Burg et al.*, 1994; *Le Hébel*, 2002]. Along most sections across the South Armorican Domain, the Lower Unit is roofed by major gently dipping extensional shear zones along which two-mica granite laccoliths emplaced during the shearing [*Gapais et al.*, 1993]. At the scale of the South Armorican Domain, the tectonic contact between the Lower and overlying units appears as plurifacial. In the southern end of the domain (i.e., in the Sables d'Olonne area), extensional tectonics is mainly accommodated by pervasive thinning of the entire metamorphic series rather than by strain localization along a major shear zone. There, homogeneous thinning leads to a drastic contraction of the metamorphic isogrades from epizonal metamorphic to partial melting conditions [*Cagnard et al.*, 2004] and the field thermal gradients locally reach transient values of the order of 70–80°C/km [*Goujou*, 1992]. The regional clustering of many isotopic ages around ~310–300 Ma in the Lower Unit suggests a relatively fast cooling [*Goujou*, 1992; *Gapais et al.*, 1993; *Brown and Dallmeyer*, 1996; *Turrillot et al.*, 2009]. Together with the widespread crustal melting, and the generalized extensional tectonics, the fast cooling rates argue for a rather fast Late Carboniferous late collisional gravitational collapse of the Variscan over-thickened continental crust [*Brown and Dallmeyer*, 1996; *Brown*, 2005]. In parallel, age of the ductile dextral motion along the South Armorican Shear Zone has also been settled by recent conventional ^{40}Ar/^{39}Ar analyses on white micas at ~310–300 Ma (G. Ruffet as cited by *Le Hébel* 2002]).

2.2. Geology of the Morbihan Area

[13] The Morbihan area appears as one of the best exposed sections of the Lower Unit roofed by two major extensional shear zones characterized by opposite kinematics and bounded to the North by the South Armorican Shear Zone [e.g., *Jégouzo*, 1980; *Gapais et al.*, 1993; *Turrillot et al.*, 2009] (Figure 1b). There, the Lower Unit consists of subvertical NW-SE striking migmatites derived from metasediments and rare Ordovician orthogneiss bodies [*Brown*, 1983; *Peucat*, 1983; *Jégouzo et al.*, 1986; *Audren*, 1987; *Jones and Brown*, 1990; *Guerrot et al.*, 1997]. Metamorphic peak conditions at ~9 kbar and 750–800°C [*Audren*, 1987; *Triboulet and Audren*, 1988; *Jones and Brown* 1989, 1990; *Brown and Dallmeyer*, 1996; *Johnson and Brown*, 2004] were followed by a nearly isothermal decompression path and a second episode of melt generation around ~4 kbar and 700–750°C [*Brown and Dallmeyer*, 1996]. Anatectic granite is widespread within the migmatite as diffuse bodies of various scales and develops North of Vannes as a 70 km-long elongated massif, regionally known as the Ste-Anne d'Auray magmatic complex [*Le Métour*, 1978; *Carron et al.*, 1994; *Augier et al.*, 2011]. The rocks of this complex appear as extremely variable in terms of texture, grain-size and modal composition particularly close to the Southern contact with the migmatites where biotite is abundant [*Audren*, 1987]. Based on Rb/Sr whole-rock and zircon U/Pb ages, partial melting was initially settled at 380–370 Ma

[*Vidal*, 1980; *Peucat*, 1983]. However, recent U-Th/Pb in situ dating of monazites from foliation-parallel leucosome bodies yielded a significantly younger age of 322 ± 3 Ma [*Turrillot et al.*, 2009], suggesting that migmatization occurred during Mid-Carboniferous times. Further south, another WNW-ESE elongated magmatic complex of about 20 × 50 km, known as the Carnac magmatic complex clearly cuts across the migmatitic foliation [*Audren and Le Métour*, 1976; *Carron et al.*, 1994; *Augier et al.*, 2011]. To the west of the study area, this complex consists of a main granitic pluton, surrounded by a pervasive dyke swarm particularly developed to the east [*Augier et al.*, 2011] (Figure 1b). There, in the Sarzeau area, the local abundance of dykes was initially mapped as another subordinate pluton [i.e., the Sarzeau granite; *Barrois*, 1897; *Cogné*, 1949; *Gapais et al.*, 1993]. The Carnac complex is made of a homogenous fine-to-medium grained granite of varying mineralogical composition including mostly biotite- (±cordierite-) granite, and two-mica granite particularly abundant in the dyke swarm in the Sarzeau area [*Le Métour*, 1978; *Carron et al.*, 1994; *Augier et al.*, 2011]. Recent monazite U-Th/Pb time constraints yielded emplacement ages of 319 ± 6 Ma, which is statistically similar to those reported for migmatization [*Turrillot et al.*, 2009; *Augier et al.*, 2011]. Southwest of our study area, field relationships between the Lower Unit-forming rocks and the Quiberon leucogranite are lacking (Figure 1b), and emplacement age of the Quiberon granite remains unknown. Nonetheless, it has been shown that the Quiberon leucogranite emplaced at the base of the Belle-Ile-en-Mer HP-LT Intermediate unit during a top-to-the-WNW shearing along the W-dipping Quiberon extensional shear zone (QSZ from *Gapais et al.* [1993]). The development of widespread S-C mylonitic fabrics has been dated between ~312 Ma to 300 Ma (^{40}Ar/^{39}Ar ages on white micas (G. Ruffet as cited by *Le Hébel* [2002]). East of our study area, the Lower Unit is roofed by the Sarzeau extensional Shear Zone (SSZ), another major mylonitic structure, characterized by a top-to-the-ESE sense of shear [*Turrillot et al.*, 2009] (Figures 1b and 1c). There, the overlying unit consists of micaschists and quartzites from the Vilaine unit [*Audren*, 1987; *Triboulet and Audren*, 1988; *Augier et al.*, 2011]. Upper amphibolite facies conditions [*Triboulet and Audren*, 1988; *Brown and Dallmeyer*, 1996] are seldom preserved within a pervasive greenschist facies sub-horizontal foliation bearing a WNW-ESE lineation also described farther south [*Audren*, 1987] and are related to the Devonian thrusting event [*Brun and Burg*, 1982; *Vauchez et al.*, 1987].

3. Field Structural Evidence and Kinematics for a Strain Continuum

[14] While the overall structure of the South Armorican domain has already been described [e.g., *Gapais et al.*, 1993] as well as the metamorphic evolution of the SBMB [e.g., *Brown*, 2005], particularly in the study area, little attention has been paid to the evolution of the extensional deformation, from ductile to brittle conditions. Systematic structural investigations were carried out on numerous outcrops of the area in order (1) to describe the succession of structures from early ductile deformational premises to late brittle normal faulting both in the footwall and the hanging
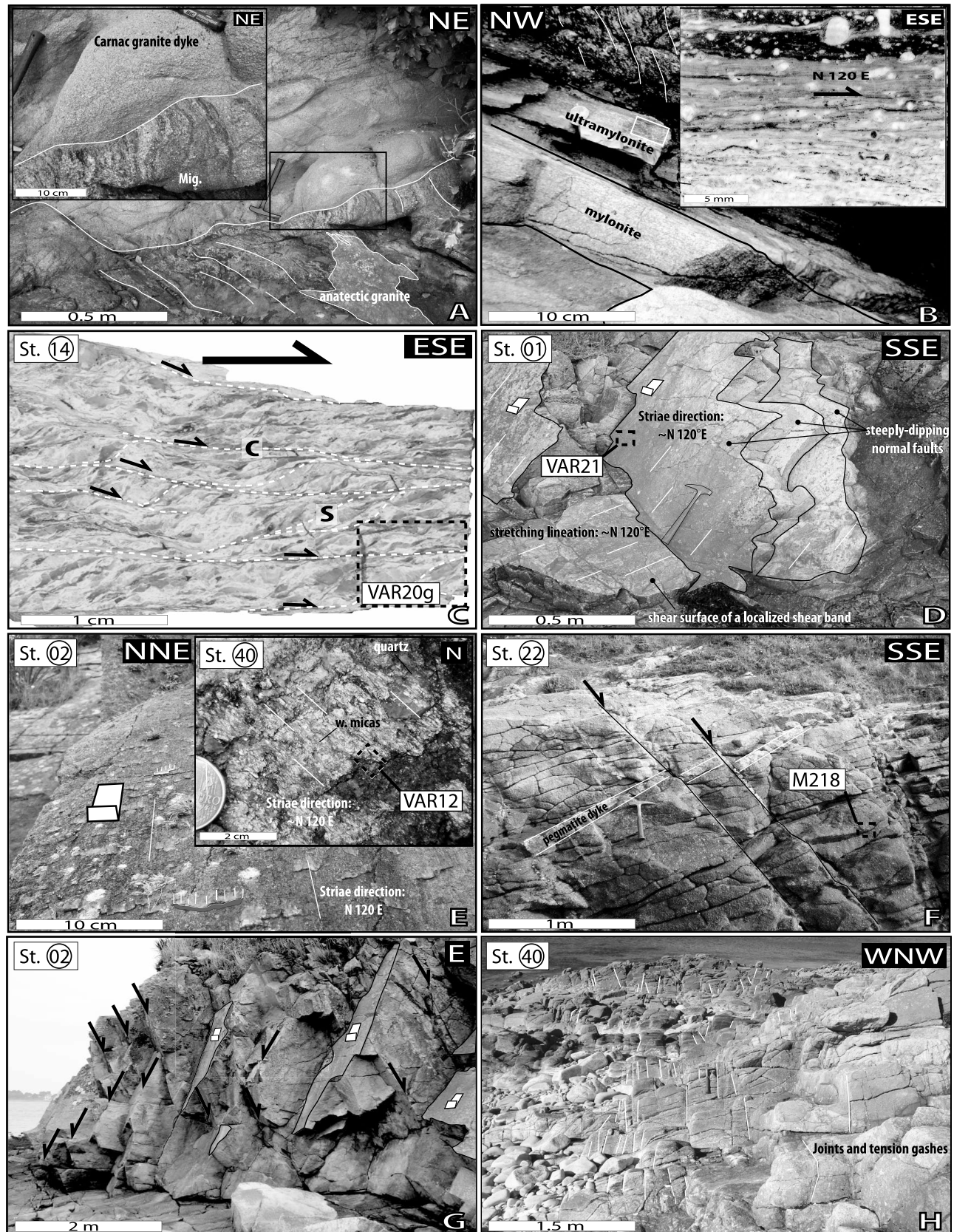
Figure 2

wall of the SSZ and (2) to settle the kinematics of each of these steps.

3.1. Early Strain Insights From the Late Migmatitic Dyke Array

[15] Granitoids are often regarded as efficient strain markers to study crustal deformation [e.g., *Brun and Pons*, 1981; *Gapais and Barbarin*, 1986; *Hibbard*, 1987; *Paterson et al.*, 1989; *Ramsay*, 1989; *Passchier*, 1990; *Faure and Pons*, 1991; *Paterson et al.*, 1998]. In particular, geometric analysis of granite dyke array has proven powerful to estimate strain main directions and ultimately the amount of strain [e.g., *Passchier*, 1990]. Occurrence of crustal extension has then been documented in the southernmost part of the Armorican Domain using an analysis of synkinematic array of granite dykes [*Cagnard et al.*, 2004].

3.1.1. Transition From Syn-to-Late Migmatitic Melt Flow Dykes

[16] A complete description of the architecture of the melt-bearing systems is beyond the scope of the present paper. Reader interested by this aspect are referred to recent studies [*Marchildon and Brown*, 2003; *Brown*, 2005] focused on key outcrops on coastal exposures of the Port-Navalo migmatites (i.e., south of the Golfe du Morbihan). The main results are discussed below.

[17] In the field, two successive generations of melt conduits can be distinguished in the Morbihan area suggesting a progressive evolution of migmatites during partial melting [*Marchildon and Brown*, 2003]. The first one consists in foliation-discordant leucosomes, characterized petrographically similar composition with the foliation-parallel leucosomes; both pertaining to the vein network developed during partial melting. In contrast, the second type of melt conduit, belonging to the Carnac complex dyke swarm is characterized by discordant granite dykes with sharp boundaries. Dykes often intersect the WNW-ESE foliation-discordant leucosomes as well as previous dykes within the migmatites (Figure 2a). Over the study area, the dyke infill is formed by consistent fine-grained granite characterized by a common assemblage of quartz, zoned plagioclase (An 15–20), K-feldspar (leading to the local development of microporphyritic texture), biotite, white mica ± cordierite. In detail, the relative proportion of white mica and biotite is variable and displays a clear evolution from biotite (±cordierite)-rich dykes preferentially encountered to the west of the Golfe du Morbihan, near the Carnac pluton, to two-mica dykes particularly abundant east of the Ile aux Moines.

3.1.2. Geometry of the Late Migmatitic Granite Dyke Swarm of the Carnac Complex

[18] At the map-scale, in the study area (Figure 1b), the dyke array crosscuts the migmatitic fabrics and forms a curved network trending ~N30–40°E to the north, ~N10–20°E in the central part of the Golfe du Morbihan and ~N00°E to N160°E to the South on the coast (Figure 1b). Away from high-strain zones, at the scale of the outcrop, the dykes are devoid of significant ductile deformation. In rare cases, a ~N120°E stretching lineation is marked by quartz-feldspar alignments. Orientation of the dyke has been measured throughout the area (Figure 3a). Statistics based on a representative population of 106 dykes (dyke width ranging from few meters to more than 500 m) indicate that the strike of dykes presents a low dispersion around a mean ~N25°E direction (Figure 3a). Poles of these dykes then appear concentrated around the principal stretching direction (X) also defined by the regional WNW-ESE lineation. The dyke-preferred orientation is thus consistent with newly formed tension-gashes developed in response to the regional WNW-ESE stretching. Furthermore, some of these dykes show an internal compositional layering parallel to the dyke borders that suggest a progressive growth during WNW-ESE stretching. Dykes are exclusively W-dipping and display a dominant sub-vertical attitude (90–80°), whereas some present a lower dip (i.e., 60–40° to 20–10°; Figure 3b).

Figure 2. Microphotographs and outcrop pictures of magmatic, ductile, ductile-brittle and brittle features. When possible either the position and the name of the sample picked for ^{40}Ar/^{39}Ar analysis or the number of the structural station (i.e., labeled "St.") are given on the pictures. Structural data and results of data inversions for these stations are given on Figure 4 for the ductile stage and on Figures 5 and 6 for brittle stage analyses. (a) Structural relationships between a steeply dipping ~N30°E striking granite dyke and the surrounding migmatites of the SBMB (vertical N120°E striking foliation). Anatectic granite bodies (Ste-Anne d'Auray granite type) are intercalated within the migmatitic foliation. Inset is a close-up view of the sharp contact between the migmatites and the dyke. (b) Decimeter-scale shear-band hosted and localized within a granite dyke, which is intensively mylonitized. Such relationships are sometimes diagnostic of a genetic link between migmatites and the foliation-discordant leucosome. Inset is a lineation-parallel oriented thin-section of ultramylonite showing unambiguous top-to-the-ESE sense of shear (e.g., δ- (delta-) type mantled porphyroclast of K-feldspar). (c) Cut and polished lineation-parallel hand-sample of mylonitized Carnac granite within the SSZ. Sense of shear is consistently top-to-the-ESE. The foliation-planes (noted "S"), the shear-planes (noted "C"), and the associated lineations have been analyzed in the station 14. (d) Overview of the station 01 displaying ductile-brittle and brittle structures. A low-angle localized shear band is cut by subsequent steeply dipping normal faults. Slip direction is ~N120°E for both ductile-brittle and brittle structures. The striated steeply dipping normal fault planes display quartz and white mica mineralizations from which the VAR21 stub had been sampled (a picture of this sample is given in Figure 9f). (e) View of a steeply dipping fault plane from station 02 showing striations and slickensides arguing for pure normal faulting. Inset is a detailed view of a normal fault plane displayed at station 40, which exhibits striated quartz and white micas crystallization (sample VAR12). (f) Displaced pegmatite layer arguing for normal faulting (station 06) in a Carnac granite dyke devoid of ductile deformation (see location on Figure 1b). Position of the M218 specimen sampled from the dyke for conventional ^{40}Ar/^{39}Ar analysis on both white micas and biotite is given. (g) Outcrop of station 02 (see map on Figure 5 for location) showing conjugated steeply dipping normal faults. (h) A narrow corridor of joints and quartz-filled tension gashes (i.e., veins) overprinting isotropic Carnac granite (from station 40, see map on Figure 6 for location).
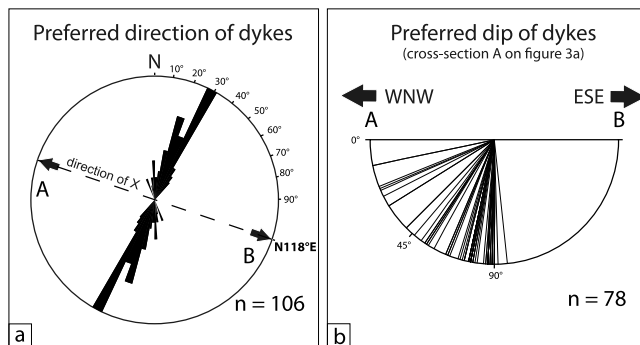
Figure 3. Results of the dyke array study. (a) Lower hemisphere projection of the orientation of dykes boundary that consistently strike N20°E–N30°E. (b) Apparent dip of the dykes projected along a stretching-parallel cross section (i.e., N115°E direction). The n indicates number of measurements; dip of some dykes has not been determined due to horizontal outcrop conditions.

Gently dipping dykes display sometimes an upward bent geometry compatible with and overall top-to-the-ESE sense of shear. However, in most cases, a progressive dyke rotation from vertical to a gently dipping position seems unlikely, as it requires a great amount of simple shear component yet not observed in the field. Then, dyke injection probably occurred with an initial west-directed dip amplified subsequently. This dyke pattern emphasizes that intrusions contribute to a late migmatitic regional WNW-ESE stretching probably accompanied by a top-to-the-ESE sense of shear.

3.2. Ductile (Mylonitic) Stage

[19] Most of the ductile deformation concentrated along the SASZ [*Jégouzo*, 1980; *Jégouzo and Rossello*, 1988] and major extensional shear zones such as the QSZ [*Gapais et al.*, 1993] and the SSZ [*Turrillot et al.*, 2009], leaving large areas where older tectonometamorphic events are preserved. Measurements on representative outcrops have been plotted on Schmidt's lower hemisphere, equal-area projection using the Tector software [*Angelier*, 1990]. Besides, for each station, stretching direction and sense of shear are reported on the map in Figure 4 and in Table 1.

[20] Zooming on the SSZ, the deformation occurs as a strain gradient over 300 to 600 m thick zone. Deformation evolves upward from weakly oriented rocks and gently E-dipping protomylonites preserving older subvertical fabrics, to mylonites and rare stripes of ultramylonite bodies (Figures 1b and 1c). There, the above mentioned Carnac dykes are mylonitized as well as the host migmatites whose inherited fabric, (i.e., regional N120°E striking vertical foliation) is strongly overprinted or even erased (Figures 1b and 1c). The mylonites were mostly formed at the expense of the Lower Unit even if a 20–50 m thick mylonitic belt also develops in the overriding Intermediate Unit made of metapelites of the SSZ hanging wall. The mylonitic foliation generally strikes NE to E, and dips gently SE (e.g., routinely 10° to 20°), and is marked by the planar alignment of quartz and feldspar porphyroclasts and white micas. The complex cartographic outline of the mylonitized zone then argues a low dip angle of the SSZ (Figure 1b) consistent with the gently dipping mylonitic fabric observed in the field. The lineation defined by stretched quartz and preferred orientation of feldspar and white mica clasts trends WNW-ESE. A general top-to-the-ESE sense of shear is determined by multiscale shear criteria; examples of kinematic criteria encountered on the field are given in inset of Figure 2b and outlined box in Figure 2c. The SSZ appears as a ductile, gently dipping extensional shear zone with a top-to-the-ESE sense of shear in its western part. Along its eastern prolongation, as the shear zone mostly trends WNW-ESE (~N120°E), this motion is accommodated by a gently south-dipping sinistral lateral ramp Figure 1b) in apparent kinematic contradiction with the SASZ (see section 5.3.).

[21] Below the SSZ, smaller ductile shear bands are scattered in the Lower Unit. In most outcrops, they display 10 cm to 1 m thick S-C mylonite bodies commonly developed in inherited anisotropies within the migmatites (Figure 2b). Mylonititic foliation, of varying attitude is generally characterized by low-angle dip (15° to 25°) and carries a pervasive WNW-ESE trending stretching lineation. Kinematic criteria such as S-C fabrics, fold asymmetry or sigma or delta-type porphyroclast systems [*Passchier and Trouw*, 1996] are consistent with an overall top-to-the-ESE sense of shear. Best-exposed examples are located on the cliffs of the Rohu cape (see location in Figure 1b). There, sills of presumably S[te]-Anne d'Auray anatectic granite are mylonitized while host rocks still strikes vertically (Figure 2b). Meter-scale flat to gently dipping (5° to 25°) localized shear bands also accumulate ductile strain (Figure 2d). Shear planes carry high-temperature striations, marked by quartz rods and fibers accompanied by neo-crystallization of syn-tectonic white micas either deformed on the shear-plane or preserved in step-shadows as rosette-shaped aggregates. Hybrid patterns of such structures argue for structures developed within the ductile-brittle transition.

[22] After emplacement of the Carnac complex dyke swarm, as temperature decreased below the granite solidus, deformation was partitioned away from the core of the Lower Unit, and was rather concentrated along the SSZ where mylonitic fabrics developed. Intense strain along the top-to-the-ESE SSZ and associated small-scale localized shear bands appears controlled by an overall WNW-ESE stretching of the entire domain.

3.3. Brittle Structures
3.3.1. Description of Brittle Structures

[23] Numerous outcrops were recognized as demonstrative of a brittle stage subsequently developed after the ductile one. The whole study area presents a pervasive steeply dipping meso- to small-scale normal fault planes network, particularly developed in the Lower Unit. Gently dipping mylonitic fabric and ductile-brittle structures are crosscut and offset by high-angle brittle normal faults (Figure 2d).

[24] Offset pegmatite dykes and well developed micro-structures such as scratches or striae, document normal faulting under brittle conditions (Figures 2e and 2f). Most outcrops display a well-expressed symmetric conjugate fault pattern (Figure 2g), while some are characterized by one dominant set of faults. No clear relation links can be proposed between faulting asymmetry and the structural position with respect to the SSZ. Furthermore, the SSZ mylonites do not present clear evidence of brittle reactiva-
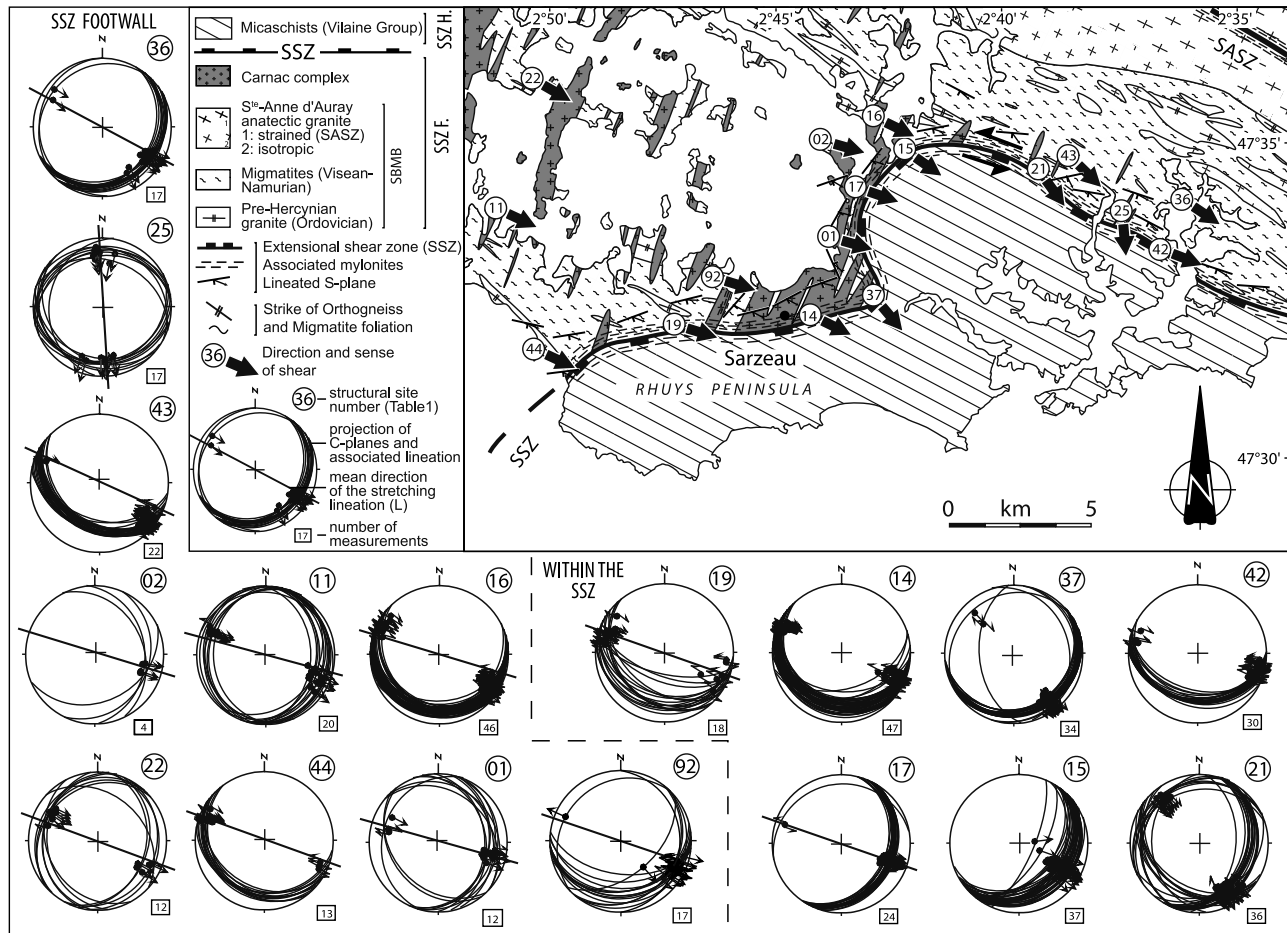
Figure 4. Analysis of ductile structures. Geological map of the SE part of the Golfe du Morbihan area where most of the ductile deformation accumulates, particularly along the SSZ (location on Figure 1b). SSZ F. and SSZ H. are for SSZ footwall and hanging wall and refer to the Lower migmatitic Unit (SBMB) and the Intermediate Unit (micaschists from the Vilaine group), respectively. The location and the results of the structural analysis of 17 sites are shown (modified from *Turrillot et al.* [2009]). Pictures of representative outcrops from the stations 14 and 01 are presented in Figures 2c and 2d, respectively. Strike of the stretching lineation and the sense of shear are indicated on the map by solid black arrows. Structural measurements were plotted using the Tector software in lower hemisphere (equal-area projection) [*Angelier*, 1990]. In strongly deformed stations (i.e., within the SSZ), bulk stretching lineation in the foliation planes is overprinted by penetrative shear planes (see mylonites in Figure 2c for example). For less deformed stations, direction of the stretching lineation is represented on stereographs by solid black lines. Complete results are given in Table 1.

tion. Only thin-layers of cataclasites occur on the secondary small-scale shear bands (e.g., Rohu cape cliffs). Slip along these faults was sometimes accompanied by a component of dilatancy as indicated by their crystallized aspect and associated veins, presumably opened as pull-aparts and filled by geodic quartz, and rosette-shaped white mica.

[25] In the SSZ hanging wall, well-expressed conjugate normal faults are rare. They are observed mainly along the Rhuys peninsula (see location in Figure 1b). There, faults often display a listric character with dip varying from 60° to less than 20° at the scale of a cliff (see detailed cross section in Figure 1c).

[26] All the geological formations around the Golfe du Morbihan are also crossed by a penetrative array of high-angle, 1 mm to 5 cm thick, quartz- (±white mica-) veins and joints arranged along narrow (e.g., 1 m to 10 m) subvertical

corridors (Figure 2h). The close association between normal fault planes and joints display contradictory intersection relationships as vertical veins cut across fault planes while some veins are crosscut by the fault planes. Vertical joints and normal faults are thus contemporaneous.

3.3.2. Fault Data Inversion

[27] The analysis of brittle structures was carried out in numerous stations away from the presumably major fault zones in order to avoid stress perturbation (Figure 5). Every station is defined as a continuous outcrop of approximately 5 to 50 m long in which brittle structures can be observed and from which the sense of slip, inferred from kinematic indicators, can be determined. 54 stations were visited and 6 to 47 measurements per station were performed. Palaeostress orientation patterns were evaluated by a computer-aided inversion method for fault slip data which is described in

Table 1. Field Data and Results of the Structural Analysis[a]

Station	Outcrop Name	Lat	Long	Lithology	N (Ductile)	Mean Direction of Transport	L	N (Brittle)	σ_1[a]	σ_2[a]	σ_3[a]	ϕ[b]	RUP %[c]	N (J. and t.-g.)	Mean Direction
1	Ludré	47° 33' 10"	−2° 44' 07"	Carnac granite (dyke)	12	N 106°E	N 104°E	26	186/82	019/08	288/02	0.428	20	22	13
2	Tascon	47° 35' 00"	−2° 44' 20"	Carnac granite (dyke)	4	N 106°E	N 106°E	40	354/85	202/05	111/02	0.345	27	42	14
3	Pointe de Penap	47° 34' 11"	−2° 51' 12"	Carnac granite (dyke)				28	092/85	217/03	307/04	0.347	28	40	30
4	Spernegy	47° 34' 44"	−2° 51' 02"	Carnac granite (dyke)				13	065/71	236/18	326/03	0.467	25	12	22
5	Brouel	47° 35' 32"	−2° 49' 46"	Carnac granite (dyke, Mig.)				13	009/81	210/08	120/03	0.401	37	27	31
6	Pointe du Trec'h	47° 36' 27"	−2° 50' 17"	Carnac granite				26	288/87	030/01	120/03	0.32	11	35	26
7	Pointe d'Aradon	47° 36' 47"	−2° 50' 08"	Carnac granite (dyke)				20	297/84	042/02	133/05	0.367	27	46	19
8	Pointe de Bénance	47° 32' 56"	−2° 46' 38"	Carnac granite (dyke, Mig.)				30	002/79	209/10	118/05	0.615	23	55	24
9	Pointe du Ruaud	47° 33' 09"	−2° 47' 12"	Carnac granite (dyke, Mig.)				16	140/88	033/01	303/02	0.537	16	41	20
10	Pointe de l'Ours	47° 33' 15"	−2° 49' 29"	Carnac granite (dyke)				24	347/82	196/07	105/04	0.557	31	54	8
11	Pointe de Kerners	47° 33' 39"	−2° 59' 39"	Carnac granite (dyke)	20	N 125°E	N 115°E	47	151/82	020/05	290/06	0.555	19	42	20
12	Pointe de Penbert	47° 33' 47"	−2° 53' 57"	Carnac granite (dyke, Mig.)				44						46	17
13	Pointe du Béché	47° 33' 03"	−2° 51' 31"	Carnac granite (dyke, Mig.)				23	080/81	221/07	311/06	0.305	22	52	36
14	Casino	47° 31' 38"	−2° 45' 06"	Ste Anne d'Auray granite	47	N 117°E[e]	N 117°E							23	43
15	Lezuis	47° 34' 25"	−2° 41' 38"	Carnac granite (dyke)	37	N 122°E[e]								57	27
16	Le Passage	47° 34' 59"	−2° 43' 39"	Carnac granite (dyke)	46	N 117°E	N 109°E	28	263/86	027/02	117/03	0.494	29	49	0
17	Lasné	47° 34' 09"	−2° 43' 39"	Carnac granite (dyke)	24	N 111°E		26	325/81	184/07	093/06	0.638	35	41	43
18	Truscat	47° 32' 37"	−2° 46' 06"	Carnac granite (dyke)				28	317/84	208/02	118/06	0.48	29	45	15
19	Le Spernec	47° 31' 35"	2° 47' 49"	Carnac granite (dyke)	18	N 105°E[e]	N 108°E							39	26
20	Cerollet	47° 32' 26"	−2° 48' 17"	Carnac granite (dyke)				35	354/82	211/17	120/05	0.581	24	47	35
21	Surzur	47° 34' 30"	−2° 38' 03"	Carnac granite (dyke)	36	N 142°E[e]		19	236/87	022/02	112/02	0.482	22	30	42
22	Port Blanc	47° 36' 08"	−2° 51' 36"	Carnac granite (dyke)	12	N 121°E	N 119°E	34	008/82	216/07	125/04	0.341	22	27	109
23	Penmern	47° 36' 59"	−2° 51' 59"	Carnac granite (dyke)				22	214/87	041/03	311/00	0.429	25	30	26
24	Séné	47° 37' 24"	−2° 45' 07"	Carnac granite				6	092/83	203/02	293/06	0.433	15	43	24
25	Tremoyec	47° 33' 36"	−2° 36' 00"	Carnac granite (dyke)	17	N 177°E[e]	N 175°E	22	105/86	198/00	288/04	0.581	9	31	31
26	Larmor Baden	47° 35' 43"	−2° 53' 34"	Carnac granite				31	173/83	025/06	295/04	0.441	10	30	19
27	Ile Berder	47° 34' 38"	−2° 53' 29"	Carnac granite				29	337/87	210/02	120/02	0.423	10	30	20
28	Pointe du Brechis	47° 35' 02"	−2° 54' 30"	Carnac granite				25	166/86	040/03	309/03	0.555	21	27	56
29	Pointe Locquemicel	47° 35' 06"	−2° 55' 25"	Carnac granite				23	265/82	049/06	139/04	0.23	21	17	49
30	La Croix Daniel (IU)	47° 30' 34"	−2° 50' 53"	Schistes				26	142/86	241/01	331/04	0.454	12		
31	Pointe Grand Mont (IU)	47° 29' 56"	−2° 50' 56"	Schistes				23	139/76	026/05	295/13	0.419	17		
32	Port Maria (IU)	47° 29' 34"	−2° 49' 58"	Schistes				24							
33	Le Pont Sal	47° 35' 02"	−2° 39' 31"	Migmatite											
34	Pointe Saint Jaques (IU)	47° 20' 09"	−2° 44' 51"	Schistes				10						17	64
35	Beg Lan (IU)	47° 30' 02"	−2° 44' 26"	Schistes										5	117
36	Billon	47° 33' 56"	−2° 34' 49"	Ste Anne d'Auray granite	17	N 125°E	N 124°E								
37	Carrière de la Motte	47° 32' 04"	−2° 42' 46"	Orthogneiss	34	N 139°E[e]									
38	Men er Belec	47° 34' 01"	−2° 59' 19"	Carnac granite				20							
39	Le Fort	47° 34' 01"	−3° 00' 16"	Carnac granite				28							
40	Pointe de Colomban	47° 33' 51"	−3° 05' 53"	Ste Anne d'Auray granite				35						18	17
41	Touchard	47° 34' 06"	−3° 05' 14"	Ste Anne d'Auray granite				24							
42	Tremoyec bis	47° 33' 35"	−2° 35' 58"	Carnac granite (dyke)	30	N 112°E[e]	N 129°E								
43	Surzur bis	47° 34' 37"	−2° 37' 29"	Carnac granite (dyke)	32	N 134°E									
44	Le Rohu	47° 31' 12"	−2° 51' 32"	Migmatite, Orthogneiss	13	N 116° E	N 115°E	25	084/84	208/03	298/05	0.818	31	22	24
45	Ty Lan	47° 36' 02"	−3° 04' 21"	Carnac granite				18							
46	Crocalan	47° 37' 22"	−3° 01' 52"	Carnac granite				14							
47	Kerlaerec	47° 36' 54"	−3° 01' 37"	Carnac granite				16							

Table 1. (continued)

| | Location | | | | Ductile Study Results | | | Brittle Study Results | | | | | | | |
| | | GPS Coordinates | | | | Mean Direction of | | | Results of Data Inversion | | | | | J. and t.-g. | |
Station	Outcrop Name	Lat	Long	Lithology	Transport	N	L	N	$\sigma_1{}^a$	$\sigma_2{}^a$	$\sigma_3{}^a$	ϕ^b	RUP %^{c}	N	Mean Direction
48	Kerisper	47° 35′ 43″	−3° 01′ 32″	Carnac granite				18							
49	Ile de Stuhan	47° 34′ 26″	−3° 02′ 42″	Carnac granite				17							
50	Le Purgatoire	47° 37′ 34″	−3° 04′ 08″	Carnac granite				20	140/88	016/01	286/01	0.395	26	29	24
51	Kerpenhir	47° 33′ 18″	−2° 55′ 48″	Carnac granite, Mig.				26	061/84	186/03	277/05	0.545	14	13	7
52	Locquidy	47° 35′ 32″	−2° 57′ 42″	Carnac granite				34	064/83	194/05	285/05	0.761	14		
53	Kerizan	47° 36′ 22″	−2° 58′ 04″	Carnac granite				24						18	29
54	Pointe Vide-Bouteille	47° 38′ 03″	−2° 57′ 50″	Carnac granite				19	306/80	039/01	130/10	0.47	21		
55	Plouhamel	47° 35′ 27″	−3° 07′ 01″	Carnac granite				20	176/80	007/10	277/02	0.563	10		
56	Porh Linemen	47° 36′ 58″	−3° 10′ 53″	Carnac granite				27	094/83	204/03	294/07	0.323	9		
57	Toulvern	47° 35′ 44″	−2° 55′ 38″	Carnac granite				26							
58	Kegenvo	47° 39′ 45″	−3° 06′ 07″	Carnac granite				18							
87	Ile de Creizic	47° 34′ 40″	−2° 52′ 06″	Carnac granite (dyke)				23	134/82	021/03	291/07	0.416	9	15	27
88	Ile de Govihan	47° 33′ 17″	−2° 50′ 47″	Carnac granite (dyke)				21	327/86	206/02	116/03	0.302	13		
89	Ile Branec	47° 33′ 43″	−2° 51′ 03″	Carnac granite (dyke)				12	088/86	207/02	298/04	0.396	18	15	34
90	Ile d'Ilur	47° 34′ 24″	−2° 47′ 43″	Carnac granite (dyke), Mig.				18	286/82	021/01	111/08	0.367	16		
91	Ile Bailleron	47° 34′ 40″	−2° 44′ 49″	Carnac granite (dyke), Mig.				12	076/84	202/04	293/05	0.353	12		
92	kervossen	47° 32′ 06″	−2° 46′ 41″	Carnac granite (dyke)	N 105°E^e	17	N 118°E								

[a]For each structural site the location, GPS coordinates and the dominant lithology are given. Depending on the nature of the deformation, ductile and/or brittle results are given. Location of the stations is shown on Figure 2. For ductile features, the direction of the stretching lineation of the bulk-rock and the sense of ductile transport over shear planes, when established, are given. For brittle structural stations, the results of computer-aided inversion (i.e. the reduce stress tensors) and the average directions of joints and tension gashes are given. Mig., migmatites; IU, Intermediate Unit; Lat, latitude and Long, longitude; N, number of measurements; L, mean direction of the stretching lineation; j. and t.-g., joints and tension gashes.

[b]The values of sigma correspond to two angles in degrees (the trend of the stress axis and its plunge).

[c]$\varphi = (\sigma_2 - \sigma_3)/(\sigma_1 - \sigma_3)$.

[d]RUP % ration of the INVDIR method [Angelier, 1990] is a quality estimator for the computed stress tensor. RUP range between 0% and 200%. Average RUP values below 50% indicate good fits between actual fault slip data and computed shear distribution.

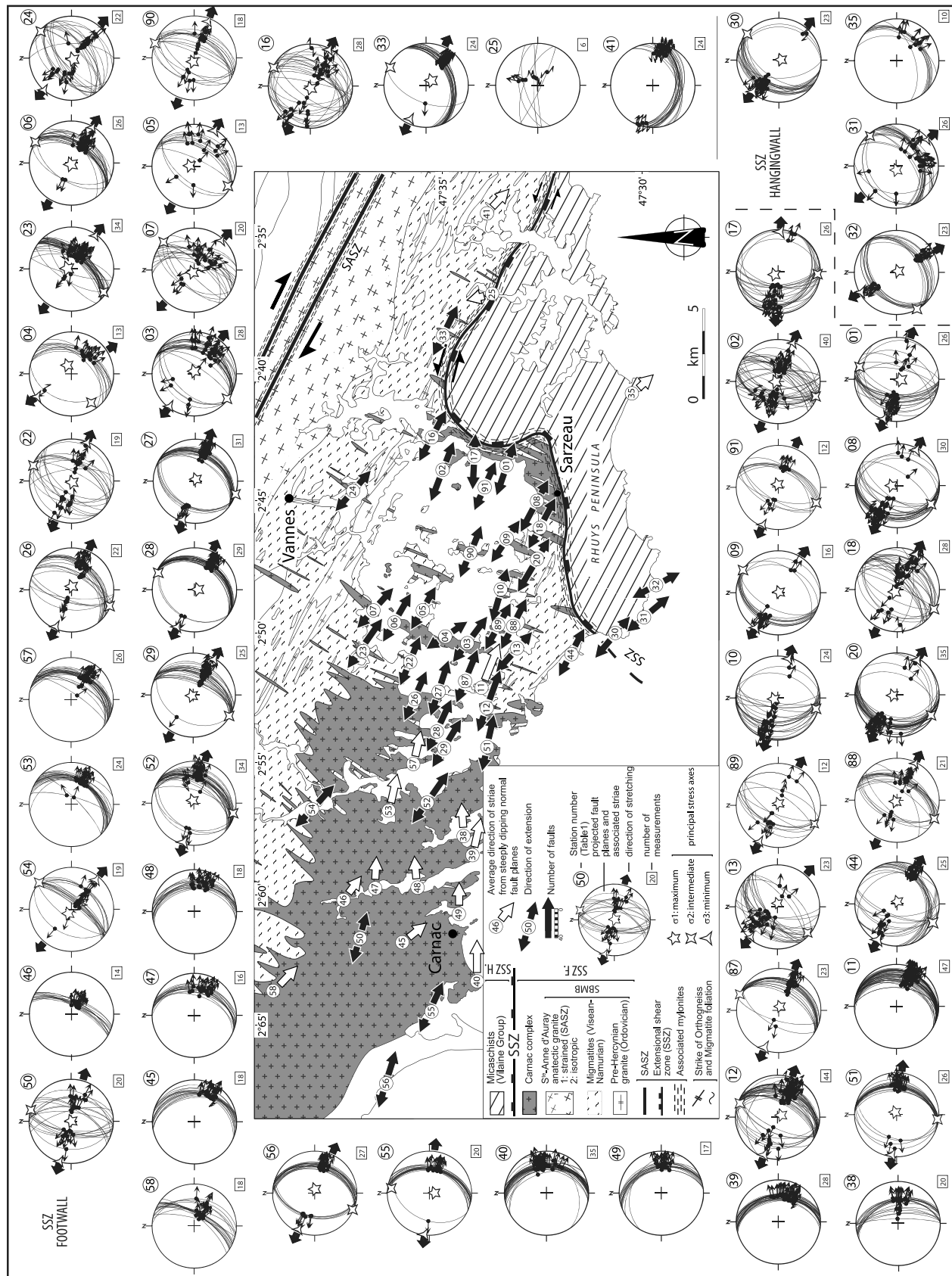[e]Average direction of transport on shear planes within the SSZ.

Figure 5

detail by *Angelier* [1984, 1990, 1994], supplemented by the analysis of veins and joints (Figure 6) [*Hancock*, 1985]. The inversion method used herein, the INVDIR program [*Angelier*, 1990], consists in the determination of the best fitting reduced paleostress tensor for 39 stations, thus identifying the orientation of the three principal stress axes ($\sigma_1 \geq \sigma_2 \geq \sigma_3$) and the ratio $\Phi = [(\sigma_2 - \sigma_3)/(\sigma_1 - \sigma_3)]$. GPS locations as well as detailed results including the orientations of the computed stress axes, and the Φ parameter are reported in Table 1 together with the statistical analysis of veins (i.e., tension gashes) and joints.

[28] In the entire studied area, the fault population is dominated by dihedral orientations and reactivated surface are rare. This fault distribution strongly argue for the formation newly formed conjugate sets of faults in isotropic to weakly anisotropic rocks and explains intermediate Φ values (i.e., 0.4 to 0.7). Results, which present low internal variations, are presented unit by unit.

[29] 1. In the Lower Unit (i.e., the SSZ footwall), 36 stations allowed the calculation of the stress tensor. In all stations, the stress tensor analysis shows a sub-vertical orientation for the maximum principal stress axis (σ_1). The minimum principal stress axis (σ_3) is horizontal or gently dipping with a consistent WNW-ESE direction since strikes range from N93°E to N146°E (Figure 5).

[30] 2. In the Intermediate Unit (i.e., SSZ hanging wall), the result of inversion also shows a sub-vertical orientation of the maximum principal stress axis (σ_1) and gently dipping orientation of the minimum principal stress axis (σ_3) striking more NW-SE (Figure 5).

[31] The plot of tension gashes and joint planes in Schmidt's lower hemisphere diagrams (equal-area projection) with the Tector software [*Angelier*, 1990] yields a consistent NNE-SSW direction (Figure 6). This trend corresponds to the calculated σ_1-σ_2 plane, and poles of the data set then appear scattered around the σ_1 axis. This geometry is in agreement with the Andersonian model for an extensional regime [*Anderson*, 1942].

[32] It is worth to note that ductile and the subsequent brittle strain structures recorded during the exhumation of the Lower Unit present a marked consistency of the stretching direction. The geometry of the Carnac complex dyke swarm, the ductile stretching lineation and the markers of extensional slip on fault planes indicate a NNE-SSW strain continuum through the ductile-brittle transition.

4. The ^{40}Ar/^{39}Ar Time Constraints

[33] Thanks to the structural guidelines detailed above where successive stages of extension and related exhumation of the continental crust were identified, a ^{40}Ar/^{39}Ar study was carried out on micas unambiguously assigned to

these different stages ranging from ductile to brittle conditions. Given the relative low thermal conditions that prevailed during the late exhumation stages (~250–450°C), in the range of the closure temperature for argon in muscovite (i.e., ~400–450°C from *Harrison et al.* [2009]), the main goal of this work was to establish an accurate link between ^{40}Ar/^{39}Ar ages and microstructures directly related to the deformation history. Therefore, samples were selected to perform in situ analysis of texturally controlled ductile and brittle features. In parallel, unstrained rocks that presumably underwent homogeneous cooling were also sampled to perform ^{40}Ar/^{39}Ar conventional analysis.

4.1. Sampling, Chemical Characterization, and Analytical Methods

4.1.1. Sampling Strategy

[34] Ten samples were selected from the Carnac granite in order to avoid problems of argon inheritance and excess argon and that could be present in minerals from the country rocks migmatites characterized by a complex tectonometamorphic history [*Brown and Dallmeyer*, 1996]. Samples were selected from key outcrops showing unambiguous deformation fabrics (e.g., Figures 2c and 2d and inset in Figure 2e), and macroscopically unaffected by meteoric weathering. Location of the dated samples is shown on Figure 1b, their relative structural position is projected onto a representative cross section (Figure 1c). To date ductile deformation (i.e., mylonitization), three samples were collected in the SSZ mylonites, two at its footwall (VAR20g and VAR24g) and one at its hanging wall (VAR20s) (Figures 9a, 9b, and 9c, respectively). Sample VAR40 comes from the shear surface of a localized shear band (Figure 9e). Three other samples (VAR21, VAR41 and VAR12; Figures 9f, 9g and 9h) were selected on steeply dipping normal fault planes characterized by white mica crystallization. To ensure a good structural control and the right target grains, thin sections were cut in the XZ plane from oriented samples containing the stretching lineation or the striation. This set of samples was completed by three samples from unstrained granitic rocks (i.e., M212, M218 and CAP03) in order to establish the cooling age of the granite through the range of the K-Ar isotopic system closure temperature for both white mica and biotite.

4.1.2. Mineral Chemistry

[35] Quantitative mineral composition of white micas and biotites were obtained with a Camebax SX50 electron microprobe co-operated by the French Geological Survey (BRGM) and ISTO (UMR CNRS 6113; Orléans). Analytic conditions were 15 kV accelerating voltage and 10 nA beam current using Fe_2O_3 (Fe), $MnTiO_3$ (Mn, Ti), diopside (Mg, Si), CaF_2 (F), orthoclase (Al, K), anorthite (Ca), albite (Na), and vanadinite (Cl) as standards. Inter- and intragrain

---

Figure 5. Analysis of brittle faults. Geological map of the whole study area encompassing both the Golfe du Morbihan and the Carnac complex area, located farther west (see location on Figure 1b). Location of the 54 stations from the Intermediate Unit and the Lower Unit where brittle analyze were carried out is shown. Pictures of representative outcrops from stations 01, 02, 22 and 40 are depicted in Figure 2. Inversion of structural data (in the sense of *Angelier* [1994]) and determination of the paleostress tensor were possible in most of the stations. Solid black arrows indicate the direction of stretching ($\sigma3$, minimum principal stress axis). Solid white arrows indicate the average of the direction of striation measured on fault planes when paleostress tensor determination was not feasible (e.g., lack of conjugate planes). The relative length of arrows indicates the number of structural measurements. Fault planes, associated striae and results of inversion were plotted using the Tector software in lower hemisphere (equal-area projection) [*Angelier*, 1990]. Complete results are given in Table 1.

Figure 6. Analysis of joints and tension gashes. Geological map is the same map as in Figure 5. Locations of the 40 stations where joints and tension gashes populations have been measured together with fault slip data are indicated. A representative picture of station 40 is shown in Figure 2h. Planes were plotted using the Tector software in lower hemisphere (equal-area projection) [*Angelier*, 1990]. Complete results are given in Table 1.
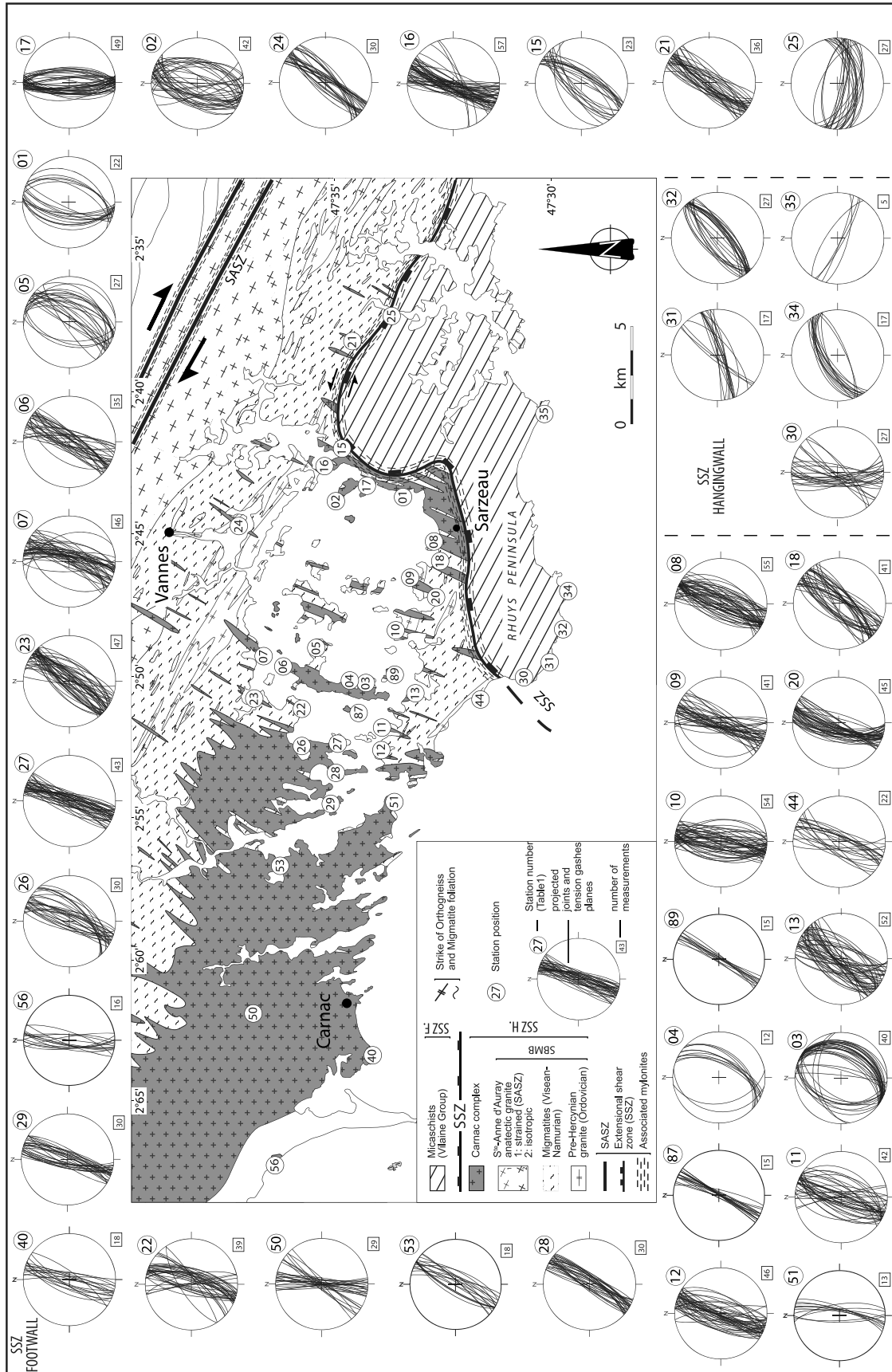
mineral composition variations were explored by X-ray mapping of 1.5×1.5 mm zones with a 512×512 pixels resolution. X-ray scan parameters were 15 kV accelerating voltage and 200 nA beam current applied during 20 ms/pixel. Textural information from Backscattered Electron (BSE) images as well as representative quantitative Electron Probe Microanalysis (EPMA) data and X-ray map are presented on Figure 7.

4.1.3. Sample Preparation, Gas Extraction Procedure, and Age Calculation

[36] Laser probe step-heating $^{40}Ar/^{39}Ar$ dating (i.e., conventional experiment) was applied on single grains of unstrained samples. Due to its high spatial resolution [e.g., *Müller*, 2003; *Mulch and Cosca*, 2004], UV-laser $^{40}Ar/^{39}Ar$ geochronology provides a powerful tool for dating different generations of the same mineral pertaining to different textural sites within deformed rocks (i.e., mylonites). This method, together with conventional method was used to set time constraints on deformed rocks from our study area. All analyses were performed at Géosciences Montpellier II (UMR 5243, CNRS) and only the main stages for sample preparation and analytical procedures for both methods are given hereafter.

[37] Single-grains were obtained by sample crushing at ~ 400 μm (jaw crusher). After purification by a Frantz magnetic barrier separator, micas were selected by manual picking using a binocular microscope. Biotite and white mica were extracted from samples M212, M218 and CAP03, with the exception of the last sample for which white micas were small and particularly rare. A white mica single-grain was also extracted manually without crushing from the protomylonite VAR21 stub to ensure a good correlation with in situ ages (Figure 9f). For deformed rocks, 1 cm^2, 1mm thick rock sections, also used to make the petrographic thin-sections were double polished to $\sim 1/4$ μm. Whole section and detailed-area photographs of both stubs and corresponding thin-sections were taken for an accurate selection of suitable areas for experiments (Figure 9). All the samples (i.e., mica single-grains and stubs) were ultrasonically rinsed in ethanol and subsequently in distilled water, wrapped in pure aluminum foils and then irradiated in the McMaster nuclear reactor (Canada) with several aliquots of the MMHb-1 international standard (i.e., 520.4 ± 1.7 Ma [*Samson and Alexander*, 1987]). After irradiation, both standards and samples were placed on a Cu-holder inside an UHV (Ultra High Vacuum) sample chamber and heated for 48 h at 150–200°C to remove adsorbed atmospheric argon from the sample and the chamber walls.

[38] Conventional experiments were conducted with a CO_2 laser operating in a continuous mode, by increasing its power at each step with an exposure time typically of 40 s for individual steps. The laser beam size was at least 2.5 times greater than the sample size in order to ensure temperature homogeneity over the whole grain. A camera placed above the sample chamber was used to monitor the temperature increase through the infrared color variations.

[39] The $^{40}Ar/^{39}Ar$ in situ laser ablation technical method was first described by *Schaeffer et al.* [1977], and the procedure was recently detailed elsewhere [*Agard et al.*, 2002; *Mulch and Cosca*, 2004; *Augier et al.*, 2005a]. Our laser system consists of a pulsed UV Nd: YAG laser and a set of lenses for beam focusing. A beam shutter allows the selection of lasering exposure time. This time depends on the nature of the analyzed mineral, its K-content (e.g., potassic white micas) and its presumed age (i.e., late Variscan). For each in situ age determination, argon was routinely extracted from a $\sim 50 \times 100$ μm surface that corresponds either to part of single-grain or to a mixture of several small grains, particularly concentrated along shear-planes. The crater produced by the laser beam is a $\sim 20–30$ μm approximate hemisphere, thus incision of the micas did not exceed 30 μm deep depending on the three-dimensional orientation of the crystals.

[40] For each experiment, once the extraction was completed, about 4 mn were required for gas cleaning within a purification line (with hot and cold traps). The purified gas was then analyzed on the electron multiplier of a MAP 215–50 noble gas mass spectrometer by peak jumping from mass 40 to mass 36 (15 runs). System blanks were routinely evaluated every three analyses and yielded values of 2×10^{-12} cm^3 for ^{40}Ar and 3×10^{-14} cm^{3}c for ^{36}Ar. For each experiment, apparent ages have been obtained after correction with blanks, mass discrimination, radioactive decay of ^{37}Ar and ^{36}Ar and irradiation-induced mass interferences. Ages have been calculated using a modified version of the Argon Integral software. Apparent ages are reported with 1σ uncertainty assuming an atmospheric composition for the initially trapped argon (i.e., $(^{40}Ar/^{36}Ar)_i \sim 295.5$) [*McDougall and Harrison*, 1999].

4.2. Mineral Habits, Textures, and Compositions

[41] White micas and biotites extracted from unstrained Carnac granite dykes are devoid of deformation and exhibit isotropic magmatic textures (see example in Figure 7a). Despite very careful sampling, biotites commonly display a slight chloritization on their rim, while white micas are preserved of any optically visible alteration traces.

[42] Samples from mylonites (VAR20g, VAR24g and VAR20s) present two different types of white mica related to the two main tectonic fabrics of the rock. Foliation planes, noted "S" (Figure 9) are marked by numerous mm-scale white mica porphyroclasts preserved as magmatic paragenesis remnants and a mixture of smaller neo-crystallized, synkinematic white micas displayed on the shear planes (noted "C"; Figures 9a, 9b, and 9c).

[43] Samples, showing ductile-brittle features (VAR40) and brittle steeply dipping normal faults (VAR41, VAR12 and VAR21), present white mica mineralization with initial sheaf-like textures (Figure 9h) locally subsequently sheared (Figures 9e, 9f, and 9g).

[44] EPMA analyses were carried out on the thin sections used for $^{40}Ar/^{39}Ar$ dating. Figure 7 displays the results obtained on biotites and on the above mentioned generations of white micas. Analyses of biotites from the samples M212, M218 and CAP03 isotropic granites display Si^{IV} contents ranging from 2.60 to ~ 2.76 cations per formula unit (c.p.f.u.) (Figure 7b). Samples M212 and M218 yield a similar range of X_{Mg} contents of the order of 0.20–0.25, whereas sample CAP03 gives higher X_{Mg} contents ($\sim 0.28–0.33$; see Figure 7b). Intrasample X_{Mg} variations might be explained by partial chloritization (Figure 7a). In contrast, inter-sample variations, as chloritization cannot be chemically demon-
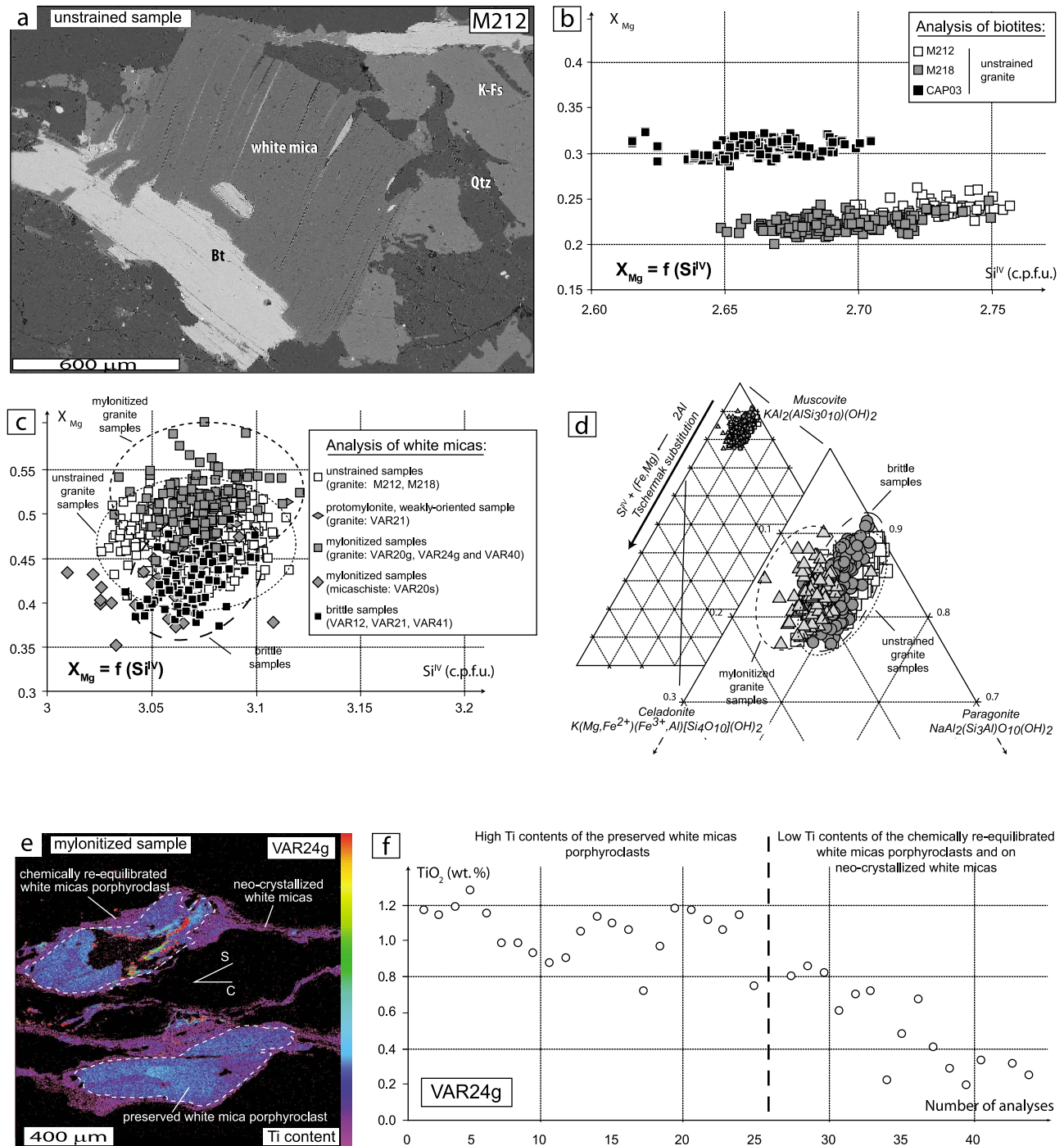
Figure 7. Main results of the mineral habits and chemical compositions analyses. (a) Mineral abbreviations are from *Kretz* [1983]. BSE (backscattered electron) image of a thin-section within the unstrained rock sample M212. Shown are white micas and biotites used for the [40]Ar/[39]Ar conventional analyses in a medium-grained magmatic isotropic texture. Note the partial disequilibrium of the edge and along the cleavage of the biotite grain. (b) Variation of X_{Mg} versus Si^{IV} contents in biotites from the dated samples obtained by EPMA analyses. Only biotites from unstrained granite have been analyzed (and then dated). (c) Variation of X_{Mg} versus Si^{IV} contents in white micas from the dated samples obtained by EPMA analyses. White micas belonging to the main deformation stages (i.e., unstrained, ductile/ductile-brittle, and brittle stages) had been analyzed. (d) Ternary composition plots for white micas belonging to unstrained (white squares), mylonitized (gray triangles) and brittle (gray circles) samples. (e) X-ray map from EPMA survey of Ti contents for the sample VAR24g. S and C refer to the foliation plane and shear plane, respectively. (f) EPMA quantitative analyses showing Ti variations in the above-described textures of with micas in sample VAR24g.
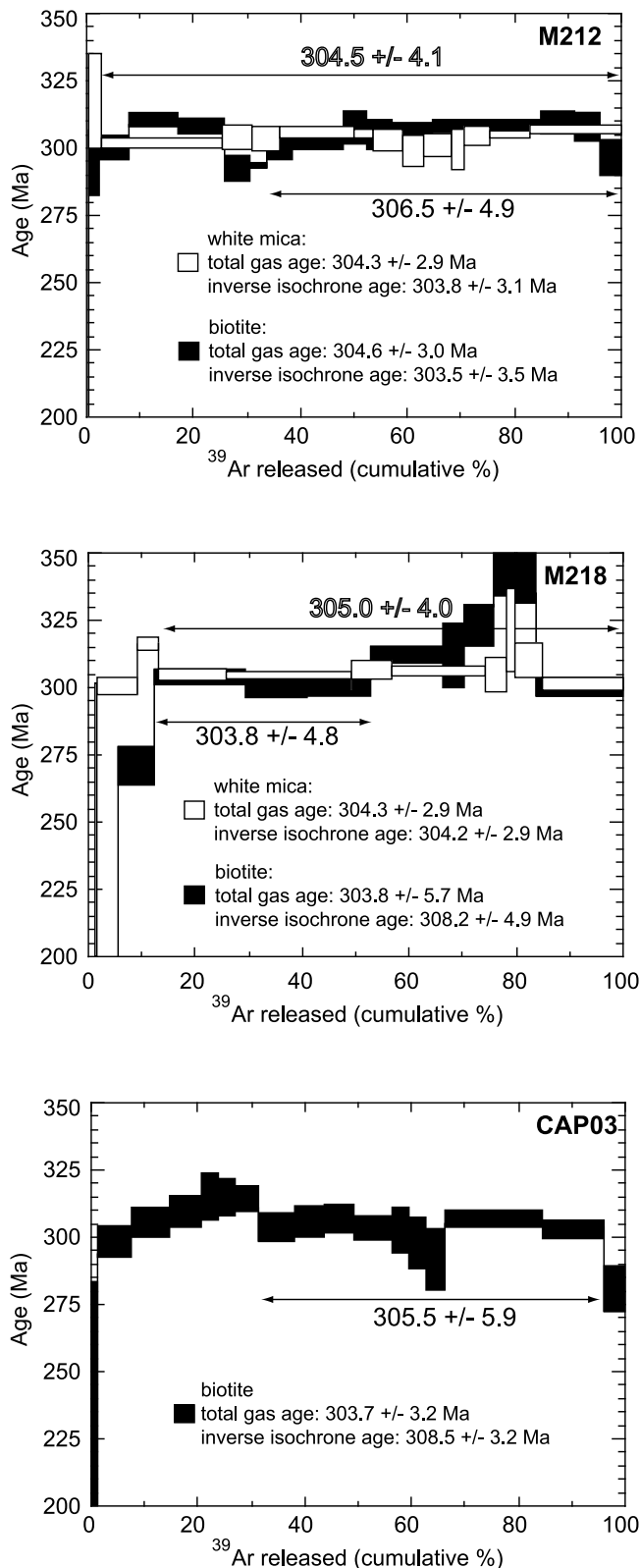
Figure 8. Results of the conventional $^{40}Ar/^{39}Ar$ (e.g., age spectra) analysis performed on white micas and biotites of unstrained samples (see location in Figure 1b), and when valid, plateau ages segment of age spectra (relative uncertainties to 2σ). Total gas and inverse isochrone ages as well as the main statistical parameters are given Table 2a.

strated (e.g., K_2O versus X_{Mg}), seem to rather highlight the overall chemical zoning of the massif [*Le Métour*, 1978; *Carron et al.*, 1994; *Augier et al.*, 2011]. At first sight, white micas analyses of all samples plot in a rather narrow range of composition, as exemplified by Si^{IV} contents comprised from 3.03 to ~3.12 c.p.f.u. (e.g., X_{Mg} versus Si^{IV} diagram, Figure 7c). In detail, despite a partial overlap, peculiar compositions can be related to the different generation of white mica identified on textural grounds (Figures 7c and 7d). For rather stable Si^{IV} contents, while unstrained granite samples yield X_{Mg} contents ranging between ~0.40 and ~0.54, whereas mylonitized samples present higher values (~0.45–0.60), and brittle samples lower values (~0.37–0.51), weakly oriented granite yielding intermediate values. Due to originally different bulk composition, mylonitized micaschists fall out of this repartition. In parallel, unstrained granite contain paragonite-rich white micas, evolving to paragonite-poor, celadonite-rich white micas in the deformed samples (Figure 7d). Conversely, samples from brittle fault planes are characterized by higher paragonite content. As Tschermak substitution ([K(Mg, Fe^{2+}) (Fe^{3+}, Al) [Si_4O_{10}] $(OH)_2$] - [$KAl_2(AlSi_3O_{10})(OH)_2$]) is generally attributed to a P increase, the composition evolution from mylonitized to brittle samples can be interpreted as due to a slight pressure decrease.

[45] In the case of mylonitized samples, X-ray maps (e.g., Ti map in Figure 7e) revealed inter- as well as intragrain chemical variations strengthened by EPMA quantitative analyses (Figure 7f). High Ti-contents preserved in white mica porphyroclasts (amounting stable ~1.1 wt% contents) are mantled by low-Ti zones, similar to synkinematic aggregates of white micas aligned in the shear planes (from around 0.8 down to 0.1 wt%). This feature argues for the neo-crystallization of white mica along the shear planed and the chemical re-equilibration of the inherited magmatic porphyroclasts during ductile deformation.

4.3. The $^{40}Ar/^{39}Ar$ Results

[46] Results of $^{40}Ar/^{39}Ar$ conventional experiments are first presented as age spectra in Figure 8, followed by the results of in situ $^{40}Ar/^{39}Ar$ analysis. Location of the white mica ablated surfaces and related in situ ages results are shown on high-resolution images of the stubs in Figure 9. Complete results of $^{40}Ar/^{39}Ar$ experiments are reported on Figure 10 and Tables 2a and 2b.

[47] Hereafter, a significant plateau age is defined by several criteria: (1) a plateau region should be constituted by a series of adjacent steps (at least three steps) that together comprise more than 50% of the total ^{39}Ar released, (2) the individual fraction ages must agree within 2σ uncertainties with the plateau age segment, and (3) one individual fraction of the plateau must comprise more than 3% of the ^{39}Ar released.

[48] For biotites, only two age spectra display significant plateau segments considering the above reported criteria. Samples M212 and CAP03 thus yield consistent plateau ages, 306.5 ± 4.9 Ma and 305.5 ± 5.9 Ma for 66% and 65% of the ^{39}Ar released respectively, in agreement with their total gas ages. The two age spectra show evidence of several disturbances, probably caused by partial chloritization of biotite and recoil phenomena during irradiation [*Lo and Onstott*, 1989]. Sample M218 shows a more disturbed age

spectrum with evidence of argon loss at the beginning of outgassing and excess argon at high experimental temperature. Three fractions give a short plateau-like segment of 303.8 ± 4.8 Ma in agreement with the total gas age (Figure 8).

[49] For white micas, the $^{40}Ar/^{39}Ar$ spectra of samples M212 and M218 show respectively simple and very well developed plateau that yield consistent ages, respectively 304.5 ± 4.1 Ma and 305.0 ± 4.0 Ma for 96% and 87% of the
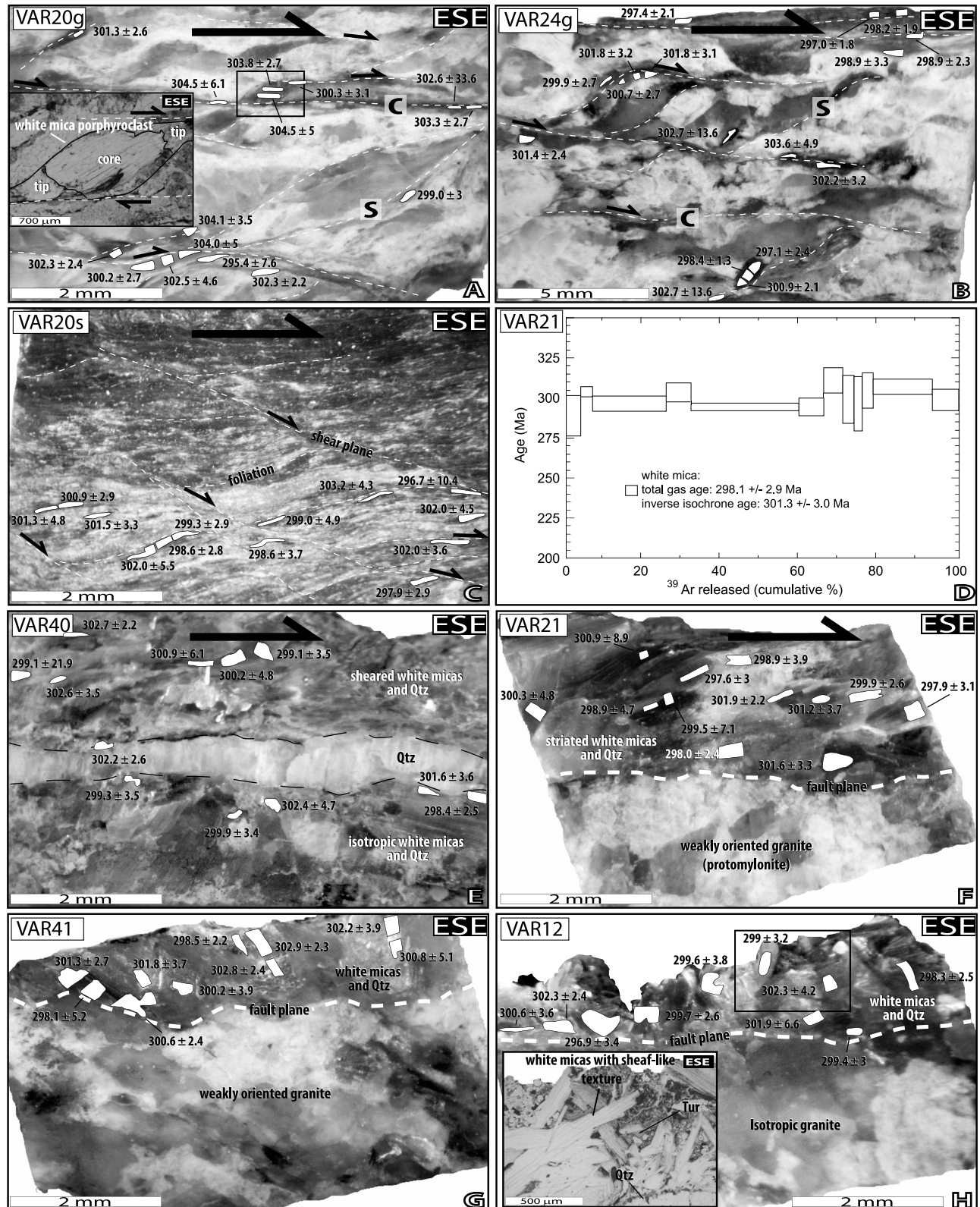

Figure 9

[39]Ar released (Figure 8). These plateau ages are consistent with their respective total gas ages.

[50] Results of in situ analyses are displayed on Figures 9 and 10 and Table 2a. Apparent ages characterized by error brackets greater than 10 Ma were not considered in the following discussion since they generally result from a too low argon volume released during laser ablation. Sample VAR20g yields ages ranging from 304.5 ± 5 Ma to 295.4 ± 7.6 Ma, with no significant variations between the different mica generations recognized on textural and chemical grounds. Inset of picture A (Figure 9) shows that the age of the mica tips (i.e., 300.3 ± 3.1 Ma) overlaps with the ages of the core (i.e., 303.8 ± 2.7 Ma and 304.5 ± 5 Ma) which indicates whether that shearing occurred during cooling of the granite or that shearing promoted a complete resetting of the original magmatic micas. For the VAR24g mylonite, the calculated ages are similar within the errors and range from 303.6 ± 4.9 Ma to 297.0 ± 1.8 Ma (Figure 9b). For the mylonitized micaschist sample VAR20s, in situ ages range from 303.2 ± 4.3 Ma to 297.9 ± 2.9 Ma (Figure 9c). For these two samples, even if punctual ages are often similar within the error brackets, the white micas belonging to the foliation planes tend to be older than micas that occur along or close to the shear planes. A control conventional [40]Ar/[39]Ar analysis was performed on a white mica from the weakly oriented granite (i.e., protomylonite) VAR21 from the SSZ mylonite belt (see location on Figures 1b, 1c and 10). The data display a disturbed age spectrum (Figure 9d) characterized by a total gas age 298.1 ± 2.9 Ma, which is significantly younger than mica ages reported above for the unstrained granitic rocks. Sample VAR40 from a ductile-brittle localized shear band, yielded in situ ages with a small scattering from 302.7 ± 2.2 Ma to 298.4 ± 2.5 Ma. Samples VAR41, VAR12, and VAR21, from high-angle normal fault planes gave all a similar, yet slightly younger, age range from 302.9 ± 2.3 Ma to 296.9 ± 3.4 Ma.

5. Discussion and Conclusions

5.1. Evidence for a WNW-ESE Homoaxial Stretching Continuum

[51] Structural analysis of ductile, ductile-brittle and brittle structures of the footwall of the Sarzeau extensional shear zone demonstrates the consistency of WNW-ESE stretching during the extensional collapse of the Variscan crust and the progressive evolution of structures from ductile to brittle. Three main steps have been recognized (Figure 10).

[52] The first step, which is the first unambiguous insight for extensional tectonics, corresponds to the emplacement of the Carnac magmatic complex and its pervasive dyke swarm. The overall geometry of the Carnac complex is characterized by a consistently striking dyke swarm around the NNE-SSW direction (~N25°E, Figure 3a) and by pluton apexes adopting the same orientation (Figure 1b). Poles of dyke surfaces are thus clustering around the principal stretch direction (X) defined by the regional WNW-ESE lineation. Furthermore, some of these dykes show internal fabrics consistent with dyke growth during the WNW-ESE stretching. Dyke intrusions thus contribute to the WNW-ESE stretching of the crust. These dykes crosscut at right angle the SBMB fabrics. Consequently, P-T conditions coeval with their emplacement are not directly known. The Carnac granite dykes post-date (1) partial melting whose P-T conditions have been estimated lower than ~4 kbar, and 700–720°C respectively, and (2) the crossing of the migmatite solidus at ~3.5 kbar and 660°C [*Brown and Dallmeyer*, 1996; *Marchildon and Brown*, 2003]. However, a progressive transition from foliation-discordant leucosomes to the sharp discordant granite dykes has been proposed for the latest evolution of the SBMB [*Marchildon and Brown*, 2003; *Brown*, 2005] highlighting a possible genetic relationship between the SBMB and the Carnac magmatic complex.

[53] During the second step, most of the ductile strain concentrated along the 300 to 600 m thick strain gradient of the SSZ characterized by a WNW-ESE stretching lineation. While the core of the Lower unit is a low-strain zone characterized by a rather coaxial component (i.e., sub-vertical dykes), deformation thus evolves toward the SSZ to a non-coaxial, top-to-the-ESE solid-state ductile shearing (Figure 10). Deformation in the SSZ hanging wall, while poorly expressed, is structurally and kinematically consistent, since part of the normal faults seems to listrically bend down on the SSZ. The total amount of displacement along the SSZ remains unknown as metamorphic contrast between both units appear, at least, partly inherited [*Triboulet and Audren*, 1985, 1988; *Brown and Dallmeyer*, 1996; *Marchildon and Brown*, 2003; *Johnson and Brown*, 2004; *Augier et al.*, 2011].

[54] During a last step, a subsequent brittle stage has been recognized. Thus, a pervasive network of steeply dipping meso- to small-scale fault planes developed crosscutting the ductile structures (Figure 10). Most of these faults are conjugate sets of faults accompanied by rare reactivated surface such as low-angle shear bands. Computer-aided inversion yielded the whole reduced stress ellipsoid characterized by a consistent horizontal WNW-ESE $\sigma3$ axis and a vertical $\sigma1$ axis (Figure 5) compatible with the NNE-SSW vertical veins and joints (Figure 6).

[55] The overall WNW-ESE stretching, first documented by the dyke swarm emplaced at depth, lasted until the complete exhumation of the SBMB under brittle conditions during the same extensional event. Crustal rock behavior thus evolved

Figure 9. Results of conventional and in situ [40]Ar/[39]Ar analysis (e.g., age spectra and laser ablation) performed on strained rocks with relative uncertainties to 1σ. Structural location of the samples is indicated on map-view (Figure 1b) and on a cross section (Figure 1c). For in situ [40]Ar/[39]Ar analyses, pictures of the whole irradiated stubs are shown, and white areas correspond to the ablated surface of white micas from which argon was extracted. Corresponding [40]Ar/[39]Ar apparent ages are given in Ma with uncertainties of 1σ. (a and b) The ductile stage issued from the SSZ mylonites; (c) Picture of mylonitized micaschists (VAR20s) from the Intermediate Unit. (d) Conventional age spectrum of protomylonite sample VAR21 picked at the base of the SSZ as a control-sample. (e) Sample VAR40, illustrating a part of a white mica-rich localized shear band of ductile-brittle character. (f–h) The brittle stage. An example of such ductile structures is displayed in Figure 2d in the station 01 (see location in Figure 5).

Figure 10. Summary of structural and age data of the distinctive deformational stages recognized in the study area. A probable scenario for the exhumation of the SBMB is also proposed. (top) Synthetic cross section (not to scale) reminding the structural relationships between the main structures encountered in the study area (position of the samples used for the $^{40}Ar/^{39}Ar$ analysis is indicated on the cross section); (middle) the integration of new conventional and in situ $^{40}Ar/^{39}Ar$ results from the geochronological analysis into the available geochronological data set. Additional geochronological data from the study area were taken from (1) *Turrillot et al.* [2009] and *Augier et al.* [2011], (2) *Brown and Dallmeyer* [1996] and (3) *Carpena et al.* [1979]; (bottom) 3D sketches that present a probable threefold scenario for the progressive exhumation of the SBMB which is partly coeval with the strain localization over the SSZ.

Table 2a. Complete Results of Conventional and In Situ ^{40}Ar/^{39}Ar Analyses[a]

Step	^{40}Ar/^{39}Ar	^{38}Ar/^{39}Ar	^{37}Ar/^{39}Ar	^{36}Ar/^{39}Ar (10^{-3})	F39Ar Released	40* (%)	40*/39K	Age (Ma)	±1σ (Ma)
				M212 White Mica					
1	32.407	0.000	0.0198	42.271	0.34	61.41	19.90	316.07	70.86
2	22.308	0.049	0.0215	41.220	0.57	45.34	10.11	167.52	118.29
3	22.392	0.011	0.0000	6.455	2.94	91.41	20.47	324.31	10.70
4	19.863	0.009	0.0000	3.131	25.50	95.26	18.92	301.73	1.76
5	19.691	0.011	0.0000	2.021	31.15	96.89	19.08	304.02	4.60
6	19.444	0.010	0.0000	1.318	36.14	97.92	19.04	303.45	4.30
7	19.661	0.010	0.0017	1.472	49.94	97.71	19.21	305.96	2.23
8	19.197	0.010	0.0000	0.000	53.67	99.92	19.18	305.53	1.59
9	19.257	0.009	0.0013	0.849	59.12	98.62	18.99	302.74	4.04
10	19.512	0.014	0.0003	2.552	63.05	96.06	18.74	299.08	5.94
11	19.362	0.008	0.0000	1.537	68.23	97.57	18.89	301.29	4.30
12	19.242	0.008	0.0034	1.567	70.65	97.51	18.76	299.40	7.37
13	19.441	0.009	0.0000	1.016	75.52	98.38	19.13	304.71	3.44
14	19.181	0.010	0.0000	0.000	82.94	99.92	19.17	305.30	1.29
15	19.776	0.011	0.00153	1.683	100.00	97.41	19.26	306.73	1.65
				M212 Biotite					
1	33.400	0.043	0.0000	71.308	0.57	36.87	12.31	200.81	41.41
2	20.217	0.023	0.0000	5.605	2.46	91.73	18.54	294.51	12.17
3	19.799	0.022	0.0000	2.828	7.85	95.70	18.95	300.40	4.60
4	19.676	0.022	0.0000	0.029	17.20	99.88	19.65	310.65	2.73
5	19.781	0.019	0.0034	0.968	25.92	98.48	19.48	308.15	2.93
6	18.516	0.019	0.0000	0.288	30.65	99.46	18.41	292.60	5.00
7	18.506	0.019	0.0000	0.000	33.68	99.92	18.49	293.71	1.15
8	19.672	0.020	0.0019	2.280	38.37	96.50	18.98	300.91	5.15
9	19.453	0.022	0.0000	1.158	48.19	98.16	19.10	302.55	2.82
10	19.583	0.020	0.0000	0.371	52.29	99.36	19.46	307.83	5.96
11	19.692	0.025	0.0000	1.395	57.14	97.83	19.26	305.01	5.47
12	19.492	0.021	0.0000	0.417	64.53	99.29	19.35	306.32	3.50
13	19.608	0.018	0.0000	0.360	85.06	99.38	19.49	308.25	2.50
14	19.682	0.022	0.0024	0.300	91.13	99.47	19.58	309.58	4.20
15	19.632	0.022	0.0027	0.458	96.06	99.23	19.48	308.17	5.25
16	19.752	0.020	0.0096	3.551	100.00	94.61	18.69	296.61	6.50
				M218 White Mica					
1	33.721	0.209	0.0000	112.960	0.14	1.0	0.33	5.71	205.01
2	24.132	0.024	0.0000	1.453	1.09	98.2	23.69	373.82	23.20
3	23.157	0.021	0.0000	22.741	1.78	70.9	16.42	267.17	34.26
4	20.567	0.013	0.0000	6.467	9.09	90.6	18.64	300.41	3.24
5	19.725	0.012	0.0000	0.000	13.26	99.9	19.71	316.21	2.22
6	19.174	0.013	0.0000	0.732	25.90	98.8	18.94	304.89	2.11
7	19.129	0.014	0.0000	0.620	49.23	99.0	18.93	304.71	1.37
8	19.746	0.013	0.0000	3.069	56.83	95.3	18.82	303.13	4.60
9	19.818	0.014	0.0090	2.599	74.11	96.0	19.04	306.26	1.89
10	19.068	0.014	0.0480	0.414	78.13	99.3	18.93	304.77	6.46
11	24.116	0.013	0.0600	13.663	79.85	83.2	20.07	321.49	15.48
12	34.13	0.021	0.0580	50.210	85.06	56.5	19.28	309.92	6.43
13	25.058	0.016	0.0290	21.418	100.00	74.7	18.72	301.53	2.38
				M218 Biotite					
1	2000.143	1.409	0.4552	6679.820	0.98	1.31	26.28	410.44	441.76
2	111.989	0.127	0.1773	332.963	5.51	12.14	13.60	223.96	20.63
3	41.009	0.051	0.1363	82.345	12.16	40.65	16.67	270.96	7.01
4	25.443	0.038	0.0140	22.175	29.19	74.19	18.88	303.90	3.05
5	23.192	0.036	0.0231	15.473	41.02	80.22	18.61	299.89	3.79
6	23.192	0.036	0.0231	15.322	52.84	80.42	18.65	300.56	3.78
7	22.244	0.039	0.0024	9.424	66.42	87.41	19.44	312.30	3.31
8	20.994	0.032	0.0378	5.283	70.12	92.50	19.42	311.96	11.87
9	22.402	0.035	0.0134	7.432	75.66	90.13	20.19	323.28	7.79
10	23.356	0.040	0.0275	5.690	79.78	92.74	21.66	344.72	10.72
11	23.588	0.035	0.0759	6.854	83.83	91.37	21.55	343.15	11.81
12	22.385	0.033	0.0235	12.633	100.00	83.26	18.64	300.39	3.56
				CAP03 Biotite					
1	21.187	0.047	0.0000	21.397	1.08	70.08	14.85	240.91	42.89
2	20.471	0.051	0.0000	5.953	7.70	91.33	18.70	298.41	5.82
3	20.022	0.050	0.0000	2.774	14.74	95.83	19.19	305.61	5.45
4	19.675	0.036	0.0000	0.645	20.64	98.95	19.47	309.74	5.83
5	20.247	0.054	0.0021	1.284	23.90	98.05	19.85	315.34	8.75
6	19.840	0.051	0.0000	0.000	27.16	99.92	19.82	314.93	6.83

Table 2a. (continued)

Step	$^{40}Ar/^{39}Ar$	$^{38}Ar/^{39}Ar$	$^{37}Ar/^{39}Ar$	$^{36}Ar/^{39}Ar$ (10^{-3})	F39Ar Released	40* (%)	40*/39K	Age (Ma)	±1σ (Ma)
7	19.803	0.054	0.0017	0.000	31.27	99.92	19.79	314.40	4.85
8	19.804	0.041	0.0000	2.486	38.09	96.21	19.05	303.67	5.42
9	19.673	0.055	0.0000	1.516	43.75	97.64	19.21	305.95	5.80
10	19.647	0.055	0.0000	1.227	49.41	98.07	19.27	306.82	5.20
11	19.390	0.050	0.0000	1.141	56.22	98.18	19.04	303.43	4.49
12	19.322	0.051	0.0076	1.091	59.34	98.25	18.98	302.65	8.49
13	19.403	0.044	0.0078	2.440	62.62	96.21	18.67	297.99	9.68
14	19.465	0.046	0.0050	4.030	66.28	93.80	18.26	291.96	11.38
15	19.284	0.061	0.0027	0.000	84.46	99.92	19.27	306.82	3.26
16	19.646	0.053	0.0047	2.119	96.02	96.74	19.00	302.94	3.70
17	19.976	0.037	0.0217	8.303	100.00	87.65	17.51	280.87	8.36
				VAR21 White Mica					
1	20.076	0.015	0.0012	6.485	3.09	90.38	18.14	290.27	8.53
2	18.862	0.009	0.0000	0.000	5.63	99.92	18.85	300.62	2.21
3	19.378	0.011	0.0018	2.982	29.95	95.37	18.48	295.25	3.17
4	19.491	0.010	0.0022	2.250	11.59	96.51	18.81	300.09	3.95
5	19.320	0.011	0.0028	3.073	56.94	95.22	18.40	294.00	1.57
6	19.232	0.012	0.0068	2.729	62.29	95.73	18.41	294.21	3.78
7	19.209	0.014	0.0000	0.125	71.30	99.73	19.16	305.16	5.24
8	19.045	0.018	0.0000	1.374	73.71	97.79	18.62	297.34	10.17
9	19.209	0.014	0.0103	2.347	75.57	96.31	18.50	295.53	11.24
10	19.140	0.008	0.0000	0.851	78.16	98.61	18.87	301.01	7.29
11	19.036	0.010	0.0017	0.081	93.35	99.79	19.00	302.83	3.18
12	18.975	0.011	0.0000	1.162	100.00	98.11	18.62	297.23	4.63
Number of Analyses	$^{40}Ar/^{39}Ar$	$^{38}Ar/^{39}Ar$	$^{37}Ar/^{39}Ar$	$^{36}Ar/^{39}Ar$ (10^{-3})	F39Ar released	40* (%)	40*/39K	Age (Ma)	±1σ (Ma)
				Var20g White Mica					
1	38.269	0.038	0.0000	65.500	0.61	49.38	18.90	302.64	33.61
2	19.657	0.015	0.0177	2.360	12.48	96.38	18.95	303.35	2.69
3	19.778	0.020	0.0000	2.510	15.50	96.17	19.02	304.45	6.15
4	20.495	0.014	0.0094	4.935	22.28	92.81	19.02	304.48	5.00
5	19.889	0.012	0.1235	3.082	28.93	95.39	18.97	303.76	2.68
6	18.896	0.012	0.0204	0.478	36.24	99.18	18.74	300.33	3.16
7	19.593	0.015	0.1435	1.992	43.18	96.97	19.00	304.18	3.50
8	18.890	0.012	0.0000	0.000	50.39	99.92	18.87	302.30	2.24
9	21.046	0.021	0.0000	8.875	52.97	87.46	18.41	295.41	7.60
10	20.800	0.017	0.0731	6.102	57.47	91.28	18.99	303.97	4.96
11	20.841	0.019	0.0506	6.576	62.83	90.62	18.89	302.48	4.51
12	19.985	0.023	0.0194	4.195	73.90	93.73	18.73	300.20	2.65
13	19.035	0.014	0.0000	0.782	83.44	98.70	18.79	301.03	2.37
14	19.573	0.013	0.0000	2.548	91.77	96.07	18.80	301.27	2.62
15	19.513	0.014	0.0000	2.868	100.00	95.58	18.65	298.99	2.99
				Var24g White Mica					
1	18.869	0.013	0.0000	1.252	9.52	97.96	18.48	296.52	1.70
2	18.623	0.014	0.0000	1.068	19.56	98.22	18.29	293.68	1.52
3	18.587	0.015	0.0281	0.100	26.96	99.77	18.54	297.42	2.15
4	18.560	0.014	0.0000	0.074	32.66	99.80	18.52	297.10	2.45
5	18.799	0.013	0.0000	0.000	38.73	99.92	18.78	300.96	2.18
6	18.625	0.011	0.0000	0.000	47.09	99.92	18.61	298.39	1.35
7	19.660	0.000	0.8676	6.935	47.33	89.83	17.67	284.45	49.83
8	21.791	0.031	0.0000	11.200	48.21	84.74	18.47	296.26	12.40
9	19.021	0.013	0.0000	1.867	55.74	97.02	18.45	296.09	2.19
10	19.339	0.011	0.0898	1.644	61.17	97.44	18.85	301.87	3.06
11	19.436	0.014	0.1364	2.008	66.62	96.92	18.84	301.78	3.19
12	19.364	0.012	0.0177	1.972	72.61	96.92	18.77	300.72	2.70
13	19.000	0.013	0.0193	1.766	78.59	97.18	18.46	296.25	2.50
14	18.984	0.013	0.0186	1.722	83.31	97.24	18.46	296.20	3.09
15	18.822	0.013	0.0053	0.791	90.07	98.68	18.57	297.85	2.21
16	19.338	0.012	0.0312	1.547	95.96	97.57	18.87	302.21	3.24
17	20.186	0.017	0.0000	4.097	98.91	93.92	18.96	303.56	4.91
18	29.104	0.022	0.0000	34.469	100.00	64.95	18.90	302.72	13.65
				Var20s White Mica					
1	19.122	0.012	0.0000	0.848	6.60	98.61	18.86	302.03	4.49
2	19.765	0.013	0.0000	3.023	13.33	95.40	18.86	302.03	3.57
3	19.897	0.015	0.0000	3.194	21.12	95.18	18.94	303.23	4.33
4	19.439	0.016	0.0000	2.607	27.11	95.96	18.65	299.03	4.98
5	19.132	0.015	0.0000	1.511	37.36	97.58	18.67	299.27	2.92

Table 2a. (continued)

Step	$^{40}Ar/^{39}Ar$	$^{38}Ar/^{39}Ar$	$^{37}Ar/^{39}Ar$	$^{36}Ar/^{39}Ar$ (10^{-3})	F39Ar Released	40* (%)	40*/39K	Age (Ma)	$\pm 1\sigma$ (Ma)
6	18.751	0.015	0.0000	0.381	48.02	99.32	18.62	298.59	2.78
7	19.394	0.017	0.0000	1.769	57.49	97.22	18.86	302.02	5.49
8	19.688	0.011	0.0000	2.881	65.74	95.60	18.82	301.52	3.33
9	19.459	0.014	0.0000	2.250	74.43	96.50	18.78	300.88	2.89
10	20.296	0.017	0.1009	5.022	79.96	92.65	18.81	301.28	4.84
11	20.232	0.017	0.0000	5.396	87.22	92.04	18.62	298.58	3.70
12	18.911	0.013	0.0000	1.072	97.31	98.24	18.58	297.93	2.93
13	25.682	0.026	0.0000	24.278	100.00	72.00	18.49	296.66	10.40
				Var40 White Mica					
1	19.624	0.015	0.0029	2.642	7.63	95.94	18.83	301.61	3.57
2	20.366	0.014	0.0388	5.902	16.64	91.37	18.61	298.40	2.49
3	19.316	0.017	0.0000	2.139	22.30	96.65	18.67	299.26	3.47
4	20.085	0.017	0.0000	4.065	29.42	93.94	18.87	302.21	2.64
5	20.172	0.014	0.0000	4.325	33.94	93.59	18.88	302.36	4.73
6	19.464	0.014	0.0000	2.493	45.13	96.14	18.71	299.90	3.41
7	19.752	0.016	0.0000	3.659	54.40	94.45	18.66	299.06	3.54
8	19.514	0.016	0.0000	2.602	59.96	95.98	18.73	300.16	4.76
9	23.762	0.017	0.0000	16.789	65.42	79.06	18.79	300.99	6.10
10	19.490	0.013	0.1071	1.967	79.41	96.98	18.90	302.71	2.21
11	18.599	0.009	0.8367	0.000	86.96	99.92	18.66	299.08	21.91
12	22.564	0.016	0.0895	12.380	100.00	83.75	18.90	302.65	3.52
				Var21 White Mica					
1	18.827	0.014	0.1867	0.835	12.74	98.68	18.58	297.96	3.17
2	19.320	0.017	0.0387	0.845	22.76	98.64	19.06	301.99	2.20
3	19.260	0.014	0.0000	2.027	31.45	96.81	18.65	298.91	3.95
4	18.600	0.013	0.0000	0.000	39.99	99.92	18.58	298.02	2.42
5	18.961	0.011	0.0000	0.083	53.37	99.79	18.92	299.98	2.60
6	18.954	0.011	0.0000	0.465	61.14	99.19	18.80	301.22	3.71
7	18.847	0.016	0.0000	0.000	68.05	99.92	18.83	301.66	3.28
8	19.148	0.013	0.0000	1.341	74.98	97.85	18.74	300.26	4.78
9	18.804	0.013	0.0000	0.785	86.68	98.68	18.56	297.60	3.02
10	19.677	0.012	0.3530	3.083	89.42	95.42	18.78	300.92	8.86
11	19.857	0.013	0.0020	3.904	93.04	94.11	18.69	299.55	7.09
12	20.388	0.012	0.1014	5.859	100.00	91.47	18.65	298.99	4.77
				Var41 White Mica					
1	19.497	0.014	0.0000	2.282	9.29	96.46	18.81	301.30	2.72
2	19.565	0.017	0.0000	3.242	18.29	95.02	18.59	298.12	5.23
3	19.086	0.012	0.0000	1.056	27.35	98.28	18.76	300.58	2.44
4	19.151	0.012	0.0000	0.747	39.46	98.77	18.92	302.90	2.34
5	19.057	0.012	0.0000	0.446	52.09	99.23	18.91	302.81	2.36
6	19.180	0.012	0.0000	0.992	59.44	98.39	18.87	302.25	3.90
7	19.451	0.021	0.0000	2.243	68.35	96.51	18.77	300.79	5.07
8	19.195	0.011	0.0000	1.159	74.18	98.13	18.84	301.75	3.72
9	19.035	0.011	0.0242	0.988	83.75	98.39	18.73	300.17	3.95
10	19.403	0.013	0.0027	2.611	100.00	95.94	18.62	298.49	2.18
				Var12 White Mica					
1	19.397	0.012	0.0000	1.029	5.52	98.35	19.08	302.26	4.18
2	19.029	0.014	0.2401	0.440	17.14	99.33	18.90	299.74	2.59
3	19.234	0.013	0.0240	1.735	28.94	97.26	18.71	296.87	3.36
4	19.312	0.014	0.0000	0.727	42.38	98.81	19.08	302.32	2.43
5	19.917	0.011	0.0800	3.720	54.35	94.43	18.81	298.35	2.54
6	19.538	0.013	0.4308	2.258	63.31	96.67	18.89	299.58	3.77
7	20.221	0.015	0.3464	4.315	73.51	93.75	18.96	300.56	3.60
8	19.548	0.014	0.0000	2.290	84.45	96.46	18.86	299.03	3.20
9	19.212	0.012	0.0605	1.089	92.77	98.27	18.88	299.39	4.01
10	20.915	0.016	0.5197	6.410	100.00	91.06	19.05	301.87	6.60

Table 2b. Sample and Conventional Analysis Parameters[a]

	J	Total Gas Age (Ma)	Inverse Isochrone Age (Ma)	$^{40}Ar/^{39}Ar$ Age (MA)	MSWD
		Sample Parameters			
M212 white mica	0.009621	304.3 ± 2.9	303.8 ± 3.1	358.7 ± 73.8	0.54
M212 biotite	0.009562	304.6 ± 3.0	303.5 ± 3.5	361.2 ± 87.3	2.76
M218 white mica	0.00972	304.3 ± 2.9	304.2 ± 2.9	298.8 ± 8.6	1.27
M218 biotite	0.00972	303.8 ± 5.7	308.2 ± 4.9	282.3 ± 6.6	6.00
CAP03 biotite	0.009621	303.7 ± 3.2	308.5 ± 3.2	195.8 ± 50.2	1.22
VAR21 white mica	0.009621	298.14 ± 2.9	301.3 ± 3.0	176.9 ± 40.4	0.82
		Analysis Parameters			
Var20g white mica	0.009665				
Var24g white mica	0.009665				
Var20s white mica	0.009665				
Var40 white mica	0.009665				
Var21 white mica	0.009665				
Var41 white mica	0.009665				
Var12 white mica	0.009561				

[a]For each sample, the J factor, the isotopic ratios and the apparent calculated ages in Ma with the corresponding errors (1σ) are given and for each conventional analysis, the total gas and inverse isochrone ages are given with the corresponding statistical parameters. F39Ar is fraction of ^{39}Ar released.

from a bulk non-localizing rheology during stretching inception at the end of partial melting, to intense strain localization over the SSZ at the ductile-brittle transition.

5.2. Time Constraints and Duration of the Extensional Tectonics

[56] Timing of deformation has been the focus of numerous studies using the complete spectrum of geochronometers. However, only rare examples provide geochronological data that can be unambiguously interpreted in terms of cooling, re-crystallization and neo-crystallization hindering definitive conclusions. Age and duration of brittle deformation is also difficult to assess and is generally constrained by indirect means such as fission tracks analysis. So far, the duration of some common geodynamic events of crustal to lithospheric-scale appears still poorly explored.

[57] Recognition of a detailed structural evolution, together with conventional and in situ $^{40}Ar/^{39}Ar$ analyses allowed placing time constraints on distinct steps of a crustal-scale stretching event, from its inception at depth to its final expression near surface.

[58] The earliest stage of crustal stretching has been recognized as the emplacement of the Carnac complex dyke swarm whose dating yielded consistent Late Carboniferous ages at around ~319 ± 6 Ma for granite emplacement (Figure 10) [*Turrillot et al.*, 2009]. These ages overlap the lower range of partial melting event settled at around ~322 ± 3 Ma and thus confirm the close link between partial melting event and magma production [*Turrillot et al.*, 2009]. Conventional $^{40}Ar/^{39}Ar$ analyses of two white mica and three biotite single grains of unstrained Carnac granite yielded consistent age spectra at ~305 ± 4 Ma for white micas and at ~304 ± 6 Ma for biotites. In parallel, syn-kinematic white mica-bearing mylonites from the SSZ were dated by in situ $^{40}Ar/^{39}Ar$ method particularly appropriate in the case of texturally complex rocks [e.g., *Agard et al.*, 2002; *Müller*, 2003; *Mulch and Cosca*, 2004; *Augier et al.*, 2005a]. Textural analysis of the deformed rocks revealed the coexistence of two generations of white micas: (1) large porphyroclasts of inherited magmatic white micas aligned along the foliation planes and (2) small syn-tectonic, neo-crystallized white mica aggregates aligned along the shear bands

(Figures 7e, 9b, and 9c). These petrographic observations have been confirmed by EPMA analyses indicating a distinct mineral chemistry for each of these populations (Figure 7). The data are mostly scattered in a narrow range of apparent ages from ~304 to 298 Ma with a routine 3 Ma error brackets. As the spatial resolution of the laser experiments does not allow a clear separation of the white mica generations, apparent ages are generally not straightforwardly consistent with the textures (Figure 9). However, these ages are consistent with the conventional age performed on the protomylonite VAR21 (Figure 9) showing a disturbed age spectrum (i.e., alternation of ~304 and ~296 Ma steps). Total gas age thus yielded an averaged yet meaningless mixture age of ~298 Ma.

[59] At high temperature, which is the case during the cooling of the Carnac granite, it is generally agreed that the closure of the K-Ar isotopic system in micas is controlled by a volume-diffusion mechanism. According to the closure temperature concept [*Dodson*, 1973], radiometric ages represent the time elapsed since the cooling through the closure temperature. This closure temperature of isotopic diffusion for white micas and biotites varies in the narrow range of 450–320°C and depends on cooling rate, grain size, and textural mineral relationships in deformed samples [*Scaillet et al.*, 1992; *Hames and Browring*, 1994; *Dahl*, 1996; *Kirschner et al.*, 1996; *Hames and Cheney*, 1997; *Villa*, 1998; *Müller*, 2003; *Mulch and Cosca*, 2004, *Augier et al.*, 2005a]. For the same magmatic body and for samples picked few kilometres apart, the closure temperature concept thus predicts that all white mica should yield the same age and this is not the case for the Carnac complex, particularly at the vicinity of the SSZ. Conversely, an overall correlation between the $^{40}Ar/^{39}Ar$ ages and the finite strain intensity toward the SSZ appear unambiguous (Figure 9). This correlation, even clear at the scale of thin-section is strengthened by changing mineral compositions.

[60] A mean age of ~305 Ma would approximate the cooling age through temperatures required for intracrystalline retention of radiogenic argon in both white micas and biotites form unstrained rocks. These ages are consistent with the 306.4 ± 0.6 Ma and 303.8 ± 0.6 Ma deduced from $^{40}Ar/^{39}Ar$ analyses performed on muscovite concentrates

from the core of the SBMB in the Golfe du Morbihan [*Brown and Dallmeyer*, 1996]. Furthermore, cooling may have been fast, as ^{40}Ar/^{39}Ar analyses on white mica and biotite yielded similar ages with respect to their error brackets. ^{40}Ar/^{39}Ar ages obtained on the mylonites, are ranging from ~304 Ma to ~298 Ma. This age scatter is interpreted as (1) successive partial isotopic and chemical re-equilibrations closely linked with strain intensity of inherited white mica porphyroclasts, and (2) neo-crystallized syn-kinematic white mica aggregates (Figures 7e and 7f). Consequently, old apparent ages (~304–302 Ma) may reflect gentle isotopic re-equilibrations of white micas (e.g., core of the grains) consistent with homogenous cooling ages obtained on unstrained rocks. Younger ages (~300–298 Ma) rather indicate either strong (i.e., total) isotopic re-equilibrations or crystallization of new white micas as suggested on Figure 7e. It is noteworthy that VAR24g displays relatively old ages when concerning (partly re-equilibrated) inherited clasts and younger ages for newly formed white mica aggregates. Thus, ductile displacement along the SSZ may have ended at around ~298 Ma, since no re-opening of the K-Ar isotopic system occurred later. A greenschist facies retrogression also occurred in the SSZ hanging wall, as evidenced by ~300–298 Ma ages obtained on mylonites developed at the expense of micaschists (sample VAR20s; see Figure 9c).

[61] The structures formed at the ductile-brittle transition or during subsequent brittle conditions are difficult to date accurately with isotopic methods because of their relative low-temperature nature, and the possible preservation of an inherited age component (e.g., clasts) [e.g., *Gibbons et al.*, 1996; *Eide et al.*, 1997; *Simon-Labric et al.*, 2009]. Localized low-angle shear bands as well as steep normal faults both carrying syn-tectonic white mica crystallizations offered the opportunity to explore the timing late ductile features activity and the formation of brittle faults. To do so, white mica crystallizations have been sampled for in situ ^{40}Ar/^{39}Ar analyses. Dated white micas mostly crystallized during displacement along fault planes (e.g., sheaf-like crystallizations into pull-apart domains on the fault plane; inset in Figure 2e and Figure 9h), some samples presenting sheared crystallizations. Furthermore, these white micas cannot be confused with clasts of the host rock, as unambiguously established by field observations and a peculiar mineral chemistry (Figures 7c and 7d). Amazingly, ^{40}Ar/^{39}Ar analyses yielded similar ~302–298 Ma ages, irrespectively to the structural relative chronology (Figure 9). This age overlap is thus interpreted here as the age of the transition from a ductile to a more brittle behavior (i.e., the ductile-brittle transition). As crystallization occurred within, or well below, the presumed closure temperature domain of muscovite, ages are interpreted as crystallization ages. A distinction between granite emplacement and tectonically controlled cooling, re-equilibration and crystallization ages has thus been univocally established. In this study, the successive phases of the same single event have been settled in terms of the deformation fabrics, kinematics and time constraints. Based on the age constraints of these three steps, duration of the late orogenic evolution and the final exhumation of the internal part of the South Armorican Variscan Belt can thus be crudely bracketed. The maximum age difference between dyke emplacement and final brittle defor-

mation spans some ~20 ± 3 My. It is noteworthy that this interval fits other late orogenic post-collisional evolution examples (e.g., the Betics [*Augier et al.*, 2005b] and the Aegean Sea [*Jolivet and Brun*, 2010]). The integration of these results in the regional context will be now described.

5.3. Regional-Scale Implications

[62] Deformation in the South Armorican Domain was initially interpreted as related to nappe-stacking during compressive tectonics [*Colchen and Poncet*, 1987]. However, more recent studies invoked a generalized orogen-parallel extension [*Gapais et al.*, 1993; *Burg et al.*, 1994; *Colchen and Rolin*, 2001; *Cagnard et al.*, 2004; *Turrillot et al.*, 2009; *Augier et al.*, 2011]. Most of these studies rely on the recognition of extensional structures such as the Quiberon shear zone [e.g., *Gapais et al.*, 1993] which provide an example of crustal-scale localized extensional shear zone or conversely, point to pervasive crustal thinning, without evidence of important detachment fault zone [*Cagnard et al.*, 2004]. In this context, this study brings new lights on the extensional tectonics in an unexplored segment of Southern Brittany.

[63] Field relationships show that the dyke intrusions occurred during a WNW-ESE large-scale stretching. While late dykes clearly cut across the migmatite foliation and part of older melt conduits some dykes are hardly distinguishable from foliation-discordant leucosomes arguing for a link between partial melting of the SBM and synkinematic granite intrusion. Stretching, initiated at depth, kept the same structural axes during the complete exhumation of the SBMB from 322 ± 6 Ma to ~302–298 Ma. Formation of the SSZ in the ongoing regional stretching, indicates strain localization over a presumably pre-existing structure (i.e., local weak heterogeneity within the ductile thickened crust) as suggested by analog models [*Brun et al.*, 1994; *Tirel et al.*, 2008]. Kinematics of the Sarzeau extensional Shear Zone indicates a top-to-the-ESE sense of shear that appears as a "conjugate" with respect to the top-to-the-WNW Quiberon Shear Zone. Both shear zones exhibit the same WNW-ESE marked stretching lineation [*Gapais et al.*, 1993; *Turrillot et al.*, 2009]. Therefore, the late orogenic evolution of the whole South Armorican Domain appears characterized by the same, consistent WNW-ESE stretching responsible for the final exhumation of the SBMB. At the scale of the entire South Armorican Domain, the mode of extension evolves from the NW where the extension is accommodated by major shear zones to the SE where pervasive crustal thinning accommodates most of the extension [*Cagnard et al.*, 2004]. Consequently, Late Variscan WNW-ESE extensional tectonics is accommodated by widespread orogen-parallel extension, which appear structurally bounded to the North by the SASZ.

[64] Homogeneous cooling of the whole SSZ footwall occurred at around ~305 Ma, as constrained by conventional ^{40}Ar/^{39}Ar on white micas and biotites whose age coincidence argues for high cooling rates. Age of the formation and activity of the SSZ and that could explain such a rapid tectonic denudation remain unsettled since only the latest deformation-related mineral re-equibrations in the mylonites have been recorded at around ~302–298Ma. Direct dating on syn-tectonic white mica crystallizations over brittle structures yielded the same narrow age range, which

is thus interpreted as the crossing of the ductile-brittle transition. The pervasive greenschists-facies retrogression that occurred in the SSZ hanging wall, is responsible for the almost total disappearance of HP/MT peak conditions assemblage equilibrated at around 8–10 kbar and 650°C [*Triboulet and Audren*, 1988; *Augier et al.*, 2011]. While metamorphic culmination may date back to ~370–350 Ma [*Bosse et al.*, 2000; *Le Hébel*, 2002; *Augier et al.*, 2011], in situ ^{40}Ar/^{39}Ar dating of white mica yielded ~300–298 Ma ages (i.e., sample VAR20s) consistent with conventional ^{40}Ar/^{39}Ar amphibole dated at ~305 Ma [*Brown and Dallmeyer*, 1996]. This result indicates a fast exhumation of this unit, which remained at a relatively deep crust level (i.e., above closure temperature of hornblende) until lately in the orogenic evolution. Furthermore, the rapid cooling at ~305 Ma of both the Lower Unit and the deepest part of the Intermediate unit appears common for the whole South Armorican Domain. In addition, this overall cooling age clusters (e.g., from NW to SE) [*Gapais et al.*, 1993; *Brown and Dallmeyer*, 1996; *Le Hébel*, 2002; *Goujou*, 1992] seem insensitive to the mode of exhumation of the metamorphic rocks [*Cagnard et al.*, 2004].

[65] Ductile dextral motion along the SASZ, which has also been settled between 310 Ma and 300 Ma, appears coeval with the extensional tectonics of the South Armorican Domain (G. Ruffet as cited by *Le Hébel* [2002]).

[66] At the light of these new results, the late evolution of this 300 km long Variscan orogenic segment of overthickened crust appears characterized by a common tectonometamorphic evolution. Exhumation of the SBMB, and more generally of the high-grade units of the variscan orogen appears controlled by the persistence of a WNW-ESE, orogen-parallel crustal stretching from ~320 Ma to ~298 Ma. The role of the SASZ that bounds these highly extended zones acted as a major orogen-parallel transfer shear zone. The connection between the SASZ and WNW-ESE extensional tectonics is beyond the scope of this paper. Nevertheless, the dextral motion along the SASZ appear linked to an overall westward tectonic escape of the South Armorican domain.

References

Agard, P., P. Monié, L. Jolivet, and B. Goffe (2002), Exhumation of the Schistes Lustrés complex: In situ laser probe ^{40}Ar/^{39}Ar constraints and implications for the Western Alps, *J. Metamorph. Geol.*, 20, 599–618, doi:10.1046/j.1525-1314.2002.00391.x.

Agard, P., L. Labrousse, S. Elvevold, and C. Lepvrier (2005), Discovery of Palaeozoic Fe-Mg carpholite (Motalafjella, Svalbard Caledonides): A milestone for subduction zone gradients, *Geology*, 33, 761–764, doi:10.1130/G21693.1.

Andersen, T. B. (1998), Extensional tectonics in the Caledonides of southern Norway, an overview, *Tectonophysics*, 285, 333–351, doi:10.1016/S0040-1951(97)00277-1.

Anderson, E. M. (1942), *The Dynamics of Faulting and Dyke Formation With Applications to Britain*, 206 pp., Olivier and Boyd, Edinburgh.

Angelier, J. (1984), Tectonic analysis of fault slip data sets, *J. Geophys. Res.*, 89(B7), 5835–5848, doi:10.1029/JB089iB07p05835.

Angelier, J. (1990), Inversion of field data in fault tectonics to obtain the regional stress. III. A new rapid direct inversion method by analytical

means, *Geophys. J. Int.*, 103, 363–376, doi:10.1111/j.1365-246X.1990.tb01777.x.

Angelier, J. (1994), Fault slips analysis and paleostress reconstruction, in *Continental Deformation*, edited by P. Hancock, pp. 53–100, Pergamon, New York.

Audren, C. (1987), Evolution structurale de la Bretagne méridionale au Paléozoïque, Ph.D. thesis, 365 pp., Univ. de Rennes 1, Rennes, France.

Audren, C., and J. Le Métour (1976), Mobilisation anatectique et déformation. Un exemple: Les migmatites du Golfe du Morbihan (Bretagne méridionale), *Bull. Soc. Geol. Fr.*, 4, 1041–1049.

Augier, R., P. Agard, P. Monié, L. Jolivet, C. Robin, and G. Booth-Rea (2005a), P-T-D-t retrograde evolution of the Nevado-Filabride complex (SE Spain): New insights from in-situ ^{40}Ar/^{39}Ar ages and metamorphic petrology, *J. Metamorph. Geol.*, 23, 357–381, doi:10.1111/j.1525-1314.2005.00581.x.

Augier, R., L. Jolivet, and C. Robin (2005b), Late orogenic doming in the eastern Betics: Final exhumation of the Nevado-Filabride complex and its relation to basin genesis, *Tectonics*, 24, TC4003, doi:10.1029/2004TC001687.

Augier, R., D. Menier, B. Van-Vliet-Lanoë, B. Hallegouët, L. Chauris, P. Turrillot, A. Carn, and I. Thinon (2011), Notice de la carte géologique de la feuille Vannes Saint-Gildas de-Rhuys à 1/50000, BRGM, Orléans, France, in press.

Axen, G. J., J. Selverstone, T. Byrne, and J. M. Fletcher (1998), If the strong crust leads, will the weak crusts follow, *GSA Today*, 8, 1–8.

Ballèvre, M., J. Marchand, G. Godard, J.-C. Goujou, and R. Wyns (1994), Eo-Hercynian events in the Armorican Massif, in *Pre-Mesozoic Geology in France and Related Areas*, edited by J. D. Keppie, pp. 183–194, Springer, Berlin.

Ballèvre, M., V. Bosse, C. Ducassou, and P. Pitra (2009), Palaeozoic history of the Armorican Massif: Models for the tectonic evolution of the suture zones, *C. R. Geosci.*, 341, 174–201, doi:10.1016/j.crte.2008.11.009.

Barrois, C. (1897), Carte géologique de la feuille de Quiberon à 1/80,000, BRGM, Orléans, France.

Berthé, D., P. Choukroune, and P. Jégouzo (1979), Orthogneiss, mylonite and non coaxial deformation of granites: The example of south Armoricain Shear Zone, *J. Struct. Geol.*, 1, 31–42, doi:10.1016/0191-8141(79)90019-1.

Bosse, V., G. Féraud, G. Ruffet, M. Ballèvre, J.-J. Peucat, and K. de Jong (2000), Late Devonian subduction and early orogenic exhumation of eclogite-facies rocks from the Champtoceaux complex (Variscan belt, France), *Geol. J.*, 35, 297–325, doi:10.1002/gj.864.

Bosse, V., M. Ballèvre, and O. Vidal (2002), Ductile thrusting recorded by the garnet isograd from blueschist-facies metapelites of the Ile de Groix, Armorican Massif, France, *J. Petrol.*, 43, 485–510, doi:10.1093/petrology/43.3.485.

Brown, M. (1983), The petrogenesis of some migmatites from the Presqu'ile de Rhuys, southern Brittany, France, in *Migmatites, Melting and Metamorphism*, edited by M. P. Atherton and C. D. Gribble, pp. 174–200, Shiva, Nantwich, U. K.

Brown, M. (2005), Synergistic effects of melting and deformation: an example from the Variscan belt, western France, *Geol. Soc. Spec. Publ.*, 243, 205–226, doi:10.1144/GSL.SP.2005.243.01.15.

Brown, M., and R. D. Dallmeyer (1996), Rapid Variscan exhumation and the role of magma in core complex formation: Southern Brittany metamorphic belt, France, *J. Metamorph. Geol.*, 14, 361–379, doi:10.1111/j.1525-1314.1996.00361.x.

Brown, M., and T. Rushmer (1997), The role of deformation in the movement of granite melt: Views from the laboratory and the field, in *Deformation-Enhanced Fluid Transport in the Earth's Crust and Mantle*, edited by M. B. Holness, pp. 111–144, Chapman and Hall, London.

Brun, J.-P., and J.-P. Burg (1982), Combined thrusting and wrenching in the Ibero-Armorican arc: A corner effect during continental collision, *Earth Planet. Sci. Lett.*, 61, 319–332, doi:10.1016/0012-821X(82)90063-2.

Brun, J.-P., and J. Pons (1981), Strain patterns of pluton emplacement in a crust undergoing non-coaxial deformation, Sierra-Morena, southern Spain, *J. Struct. Geol.*, 3, 219–229, doi:10.1016/0191-8141(81)90018-3.

Brun, J.-P., D. Sokoutis, and J. Van Den Driessche (1994), Analogue modelling of detachment fault systems and core complexes, *Geology*, 22, 319–322, doi:10.1130/0091-7613(1994)022<0319:AMODFS>2.3.CO;2.

Buck, W. R. (1991), Modes of continental lithospheric extension, *J. Geophys. Res.*, 96, 20,161–20,178, doi:10.1029/91JB01485.

Burg, J.-P., J. Van Den Driessche, and J.-P. Brun (1994), Syn- to post-thickening extension in the Variscan Belt of western Europe: Modes and structural consequences, *Geol. Fr.*, 3, 33–51.

Cagnard, F., D. Gapais, J.-P. Brun, C. Gumiaux, and J. Van Den Driessche (2004), Late pervasive crustal-scale extension in the south Armorican Hercynian belt (Vendée, France), *J. Struct. Geol.*, 26, 435–449, doi:10.1016/j.jsg.2003.08.006.

Carpena, J., D. Chaillou, A. Chambaudet, and G. Poupeau (1979), Fission track geochronology of the Hercynian Platform in France, Report of the 10th International Conference on Solid State Nuclear Track Detectors, Space Biophys. of the Parliament of the Counc. of Eur., Lyon, France.

Carron, J.-P., M. Le Guen de Kerneizon, and H. Nachit (1994), Variscan granites from Brittany, in *Pre-Mesozoic Geology in France and Related Areas*, edited by J. D. Keppie, pp. 231–239, Springer, Berlin.

Charles, N., et al. (2011), Metamorphic Core Complexes vs. synkinematic plutons in continental extension setting: Insights from key structures (Shandong Province, eastern China), *J. Asian Earth Sci.*, 40, 261–278, doi:10.1016/j.jseaes.2010.07.006.

Cocherie, A., E. Be Mezeme, O. Legendre, M. Fanning, M. Faure, and P. Rossi (2005), Electron microprobe dating as a tool for understanding closure of U-Th-Pb system in monazite from migmatite, *Am. Mineral.*, 90, 607–618, doi:10.2138/am.2005.1303.

Cogné, J. (1949), Quelques observations tectoniques sur les schistes cristal-lins et les granites de la Cornouaille maritime, *C. R. Hebd. Seances Acad. Sci.*, 229, 1251–1253.

Cogné, J. (1974), Le Massif armoricain, in *Géologie de la France*, edited by J. Debelmas, pp. 105–161, Doin, Paris.

Colchen, M., and D. Poncet (1987), Sur l'âge post-Tournaisien de la tectonique synshisteuse à Brétignolles-sur-Mer, Vendée littorale, Massif Armoricain, *C. R. Acad. Sci.*, 305, 1255–1258.

Colchen, M., and P. Rolin (2001), La chaîne hercynienne en Vendée, *Geol. Fr.*, 2, 53–85.

Corti, G., M. Bonini, S. Conticelli, F. Innocenti, P. Manetti, and D. Sokoutis (2003), Analogue modelling of continental extension: A review focused on the relations between the patterns of deformation and the presence of magma, *Earth Sci. Rev.*, 63, 169–247, doi:10.1016/S0012-8252(03)00035-7.

Dahl, P. S. (1996), The crystal-chemistry basis for Ar retention in micas: Inferences from interlayer partitioning and implications for geochronology, *Contrib. Mineral. Petrol.*, 123, 22–39, doi:10.1007/s004100050141.

Davy, P., A. Hansen, E. Bonnet, and S. Z. Zhang (1995), Localization and fault growth in layered brittle-ductile systems: Implications for deformations of the continental lithosphere, *J. Geophys. Res.*, 100, 6281–6294, doi:10.1029/94JB02983.

Dodson, M. (1973), Closure temperature in cooling geochronological and petrological systems, *Contrib. Mineral. Petrol.*, 40, 259–274, doi:10.1007/BF00373790.

Eide, E. A., T. H. Torsvik, and T. B. Andersen (1997), Absolute dating of brittle fault movements: Late Permian and late Jurassic extensional fault breccias in western Norway, *Terra Nova*, 9, 135–139, doi:10.1046/j.1365-3121.1997.d01-21.x.

Faure, M., and J. Pons (1991), Crustal thinning recorded by the shape of the Namurian-Westphalian leucogranite in the Variscan Belt of the north-west Massif Central, France, *Geology*, 19, 730–733, doi:10.1130/0091-7613(1991)019<0730:CTRBTS>2.3.CO;2.

Faure, M., W. Lin, L. Shu, Y. Sun, and U. Schärer (1999), Tectonics of the Dabieshan (eastern China) and possible exhumation mechanism of ultra high-pressure rocks, *Terra Nova*, 11, 251–258, doi:10.1046/j.1365-3121.1999.00257.x.

Faure, M., E. Be Mézeme, M. Duguet, C. Cartier, and J.-Y. Talbot (2005), Paleozoic tectonic evolution of medio-Europa from the example of the French Massif Central and Massif Armoricain, *J. Virtual Expl.*, 19, Paper 5.

Faure, M., E. Be Mezeme, A. Cocherie, P. Rossi, A. Chemenda, and D. Boutelier (2008), Devonian geodynamic evolution of the Variscan Belt, insights from the French Massif Central and Massif Armoricain, *Tectonics*, 27, TC2005, doi:10.1029/2007TC002115.

Gapais, D., and B. Barbarin (1986), Quartz fabric transition in a cooling syntectonic granite (Hermitage Massif, France), *Tectonophysics*, 125, 357–370, doi:10.1016/0040-1951(86)90171-X.

Gapais, D., J.-L. Lagarde, C. Le Corre, C. Audren, P. Jégouzo, A. Casas Sainz, and J. Van Den Driessche (1993), La zone de cisaillement de Quiberon: Témoin d'extension de la chaîne Varisque en Bretagne méridionale au Carbonifère, *C. R. Acad. Sci.*, 316, 1123–1129.

Gibbons, W., R. Doig, T. Gordon, B. Murphy, P. Reynolds, and J. Clancy (1996), Mylonite to megabreccia: Tracking fault events within transcurrent terrane boundary in Nova Scotia, *Can. Geol.*, 24, 411–414.

Goujou, J.-C. (1992), Analyse pétro-structurale dans un avant-pays métamorphique: Influence du plutonisme tardi-orogénique Varisque sur l'encaissant épi à mésozonal de Vendée, 216 pp., BRGM, Orléans, France.

Guerrot, C., F. Béchennec, and D. Thiéblemont (1997), Le magmatisme paléozoïque de la partie nord-ouest du domaine sud-armoricain données géochronologiques nouvelles, *C.R. Acad. Sci.*, 324, 977–984.

Gumiaux, C., J.-P. Brun, and D. Gapais (2004), Strain removal within the Hercynian Shear Belt of central Brittany (western France): Methodology and tectonic implications, *Geol. Soc. Spec. Publ.*, 224, 287–305, doi:10.1144/GSL.SP.2004.224.01.18.

Hames, W. E., and S. A. Browring (1994), An empirical evaluation of the Argon diffusion geometry in muscovite, *Earth Planet. Sci. Lett.*, 124, 161–169, doi:10.1016/0012-821X(94)00079-4.

Hames, W. E., and J. T. Cheney (1997), On the loss of ^{40}Ar from muscovite during polymetamorphism, *Geochim. Cosmochim. Acta*, 61, 3863–3872, doi:10.1016/S0016-7037(97)00207-X.

Hancock, P. L. (1985), Brittle microtectonics: Principles and practice, *J. Struct. Geol.*, 7, 437–457, doi:10.1016/0191-8141(85)90048-3.

Handy, M. R., and J.-P. Brun (2004), Seismicity, structure and strength of the continental lithosphere, *Earth Planet. Sci. Lett.*, 223, 427–441, doi:10.1016/j.epsl.2004.04.021.

Harrison, T. M., J. Celerier, A. B. Aikman, J. Hermann, and T. Matthew (2009), Diffusion of ^{40}Ar in muscovite, *Geochim. Cosmochim. Acta*, 73, 1039–1051, doi:10.1016/j.gca.2008.09.038.

Hibbard, M. (1987), Deformation of incompletely crystallized magma systems: Granitic gneisses and their tectonic implications, *J. Geol.*, 95, 543–561, doi:10.1086/629148.

Hollister, L. S. (1993), The role of melt in the uplift and exhumation of orogenic belts, *Chem. Geol.*, 108, 31–48, doi:10.1016/0009-2541(93)90316-B.

Iglesias, M., and J.-P. Brun (1976), Signification des variations et anomalies de la déformation dans un segment de la chaîne hercynienne (les séries cristallophylliennes de la Vendée littorale, Massif Armoricain), *Bull. Soc. Geol. Fr.*, 18, 1443–1452.

Jégouzo, P. (1980), The South Armorican shear zone, *J. Struct. Geol.*, 2, 39–47, doi:10.1016/0191-8141(80)90032-2.

Jégouzo, P., and E. A. Rossello (1988), La Branche Nord du Cisaillement Sud-Armoricain (France): Un essai d'évaluation du déplacement par l'analyse des mylonites, *C.R. Acad. Sci.*, 307, 1825–1831.

Jégouzo, P., J.-J. Peucat, and C. Audren (1986), Caractérisation et signification géodynamique des orthogneiss calco-alcalins d'âge ordovicien de Bretagne méridionale, *Bull. Soc. Geol. Fr.*, 2, 839–848.

Johnson, T., and M. Brown (2004), Quantitative constraints on metamorphism in the Variscides of southern Brittany—A complementary pseudo-section approach, *J. Petrol.*, 45, 1237–1259, doi:10.1093/petrology/egh012.

Jolivet, L., and J.-P. Brun (2010), Cenozoic geodynamic evolution of the Aegean, *Int. J. Earth Sci.*, 99, 109–138, doi:10.1007/s00531-008-0366-4.

Jolivet, L., C. Faccenna, B. Goffé, E. Burrov, and P. Agard (2003), Subduction tectonics and exhumation of high-pressure metamorphic rocks in the Mediterranean orogens, *Am. J. Sci.*, 303, 353–409, doi:10.2475/ajs.303.5.353.

Jolivet, L., H. Raimbourg, L. Labrousse, D. Avigad, Y. Leroy, H. Austrheim, and T. B. Andersen (2005), Softening triggered by eclogitization, the first step toward exhumation during continental subduction, *Earth Planet. Sci. Lett.*, 237, 532–547, doi:10.1016/j.epsl.2005.06.047.

Jones, K. A., and M. Brown (1989), The metamorphic evolution of the Southern Brittany Migmatite Belt, *Geol. Soc. Spec. Publ.*, 43, 501–505, doi:10.1144/GSL.SP.1989.043.01.47.

Jones, K. A., and M. Brown (1990), High-temperature 'clockwise' P-T paths and melting in the development of regional migmatites: An example from southern Brittany, France, *J. Metamorph. Geol.*, 8, 551–578, doi:10.1111/j.1525-1314.1990.tb00486.x.

Kirschner, L., M. A. Cosca, H. Masson, and J. C. Hunziker (1996), Staircase ^{40}Ar/^{39}Ar spectra of fine-grained white mica: Timing and duration of deformation and empirical constraints on argon diffusion, *Geology*, 24, 747–750, doi:10.1130/0091-7613(1996)024<0747:SAASOF>2.3.CO;2.

Kretz, R. (1983), Symbols of rock forming minerals, *Am. Mineral.*, 68, 277–279.

Labrousse, L., L. Jolivet, P. Agard, R. Hébert, and T. B. Andersen (2002), Crustal-scale boudinage and migmatization of gneiss during their exhumation in the UHP province of western Norway, *Terra Nova*, 14, 263–270, doi:10.1046/j.1365-3121.2002.00422.x.

Le Corre, C., B. Auvray, M. Ballevre, and M. Robardet (1991), Le Massif Armoricain, *Sci. Geol. Bull.*, 44, 31–103.

Le Hébel, F. (2002), Déformation continentale et histoire des fluides au cours d'un cycle subduction, exhumation, extension. Exemples des porphyroïdes sud-armoricains, Ph.D. thesis, 250 pp., Univ. de Rennes, Rennes, France.

Le Hébel, F., O. Vidal, J.-R. Kienast, and D. Gapais (2002b), Les 'Porphyroïdes' de Bretagne méridionale: Une unité de HP-BT dans la chaine hercynienne, *C. R. Geosci.*, *334*, 205–211.

Le Métour, J. (1978), Petrogenesis of migmatites and associated granites in south Brittany, *Neues Jahrb. Mineral. Monatsh.*, *8*, 364–376.

Lister, G. S., G. Banga, and A. Feenstra (1984), Metamorphic core complexes of cordilleran type in the Cyclades, Aegean Sea, Greece, *Geology*, *12*, 221–225, doi:10.1130/0091-7613(1984)12<221:MCCOCT>2.0. CO;2.

Lo, C. H., and T. C. Onstott (1989), ^{39}Ar recoil artefacts in chloritized biotite, *Geochim. Cosmochim. Acta*, *53*, 2697–2711, doi:10.1016/0016-7037(89)90141-5.

Malavieille, J. (1993), Late orogenic extension in mountain belts: Insights from the Basin and Ranges and the Late Paleozoic Variscan Belt, *Tectonics*, *12*, 1115–1130, doi:10.1029/93TC01129.

Marchand, J. (1981), Ecaillage d'un mélange tectonique profond: Le complexe cristallophyllien de Champtoceaux (Bretagne méridionale), *C.R. Acad. Sci.*, *293*, 223–228.

Marchildon, N., and M. Brown (2003), Spatial distribution of melt-bearing structures in anatectic rocks from southern Brittany, France: Implications for melt-transfer at grain-scale to orogen-scale, *Tectonophysics*, *364*, 215–235, doi:10.1016/S0040-1951(03)00061-1.

Matte, P. (1986), La chaîne Varisque parmi les chaînes Paléozoïques péri atlantiques, modèle d'évolution et position des grands blocs continentaux au Permo-Carbonifère, *Bull. Soc. Geol. Fr.*, *2*, 9–24.

Matte, P. (2001), The Variscan collage and orogeny (480–290 Ma) and the tectonic definition of the Armorica microplate: A review, *Terra Nova*, *13*, 122–128, doi:10.1046/j.1365-3121.2001.00327.x.

Maurel, O., P. Monié, J.-P. Respaut, A. F. Leyreloup, and H. Maluski (2003), Pre-metamorphic ^{40}Ar/^{39}Ar and U-Pb ages in HP metagranitoïds from the Hercynian belt (France), *Chem. Geol.*, *193*, 195–214, doi:10.1016/S0009-2541(02)00351-0.

McDougall, I., and T. M. Harrison (1999), *Geochronology and Thermochronology by the ^{40}Ar/^{39}Ar Method*, 282 pp., Oxford Univ. Press, New York.

Mulch, A., and M. A. Cosca (2004), Recrystallization or cooling ages: In situ UV-laser ^{40}Ar/^{39}Ar geochronology of muscovite in mylonitic rocks, *J. Geol. Soc.*, *161*, 573–582, doi:10.1144/0016-764903-110.

Müller, W. (2003), Strengthening the link between geochronology, textures and petrology, *Earth Planet. Sci. Lett.*, *206*, 237–251, doi:10.1016/S0012-821X(02)01007-5.

Passchier, C. W. (1990), Reconstruction of deformation and flow parameters from deformed vein sets, *Tectonophysics*, *180*, 185–199, doi:10.1016/0040-1951(90)90307-T.

Passchier, C. W., and R. A. J. Trouw (1996), *Microtectonics*, 289 pp., Springer, Berlin.

Paterson, S. R., R. H. Vernon, and O. T. Tobisch (1989), A view of criteria for the identification of magmatic and tectonic foliations in granitoïds, *J. Struct. Geol.*, *11*, 349–363, doi:10.1016/0191-8141(89)90074-6.

Paterson, S. R., T. K. Fowler, K. L. Schmidt, A. S. Yoshinobu, E. S. Yuan, and R. B. Miller (1998), Interpreting magmatic fabric patterns in plutons, *Lithos*, *44*, 53–82, doi:10.1016/S0024-4937(98)00022-X.

Peucat, J.-J. (1983), Géochronologie des roches métamorphiques (Rb-Sr et U-Pb). Exemples choisis au Groënland, en Laponie, dans le Massif armoricain et en Grande Kabylie, *Mem. Soc. Geol. Mineral. Bretagne*, *28*, 158 pp.

Platt, J. L. (1986), Dynamics of orogenic wedges and the uplift of high-pressure metamorphic rocks, *Geol. Soc. Am. Bull.*, *97*, 1037–1053.

Ramsay, J. G. (1989), Emplacement kinematics of a granite diapir: The Chindamora Batholith, Zimbabwe, *J. Struct. Geol.*, *11*, 191–209, doi:10.1016/0191-8141(89)90043-6.

Ranalli, G. (1997), Rheology of the lithosphere in space and time, *Geol. Soc. Spec. Publ.*, *121*, 19–37, doi:10.1144/GSL.SP.1997.121.01.02.

Ranalli, G. (2003), How soft is the crust?, *Tectonophysics*, *361*, 319–320, doi:10.1016/S0040-1951(02)00607-8.

Rey, P., O. Vanderheaghe, and C. Teyssier (2001), Gravitational collapse of continental crust: Definition, regimes, and modes, *Tectonophysics*, *342*, 435–449, doi:10.1016/S0040-1951(01)00174-3.

Rey, P., C. Teyssier, and D. L. Whitney (2009), The role of partial melting and extensional strain rates in the development of metamorphic core complexes, *Tectonophysics*, *477*, 135–144, doi:10.1016/j.tecto.2009.03.010.

Samson, S., and E. C. Alexander (1987), Calibration of the interlaboratory ^{40}Ar-^{39}Ar dating standard, MMhb-1, *Isot. Geosci.*, *66*, 27–34, doi:10.1016/0168-9622(87)90025-X.

Scaillet, S., G. Feraud, M. Ballèvre, and M. Amouric (1992), Mg/Fe and (Mg, Fe) Si-Al$_2$ compositional control on argon behaviour in high-pressure white micas: A ^{40}Ar/^{39}Ar continuous laser-probe study from the Dora-Maira nappe of the internal western Alps, Italy, *Geochim. Cosmochim. Acta*, *56*, 2851–2872, doi:10.1016/0016-7037(92)90364-O.

Schaeffer, O. A., W. Müller, and T. V. Grove (1977), Laser Ar/Ar study of Apollo 17 basalts, *Geochim. Cosmochim. Acta*, *8*, 1489–1499.

Simon-Labric, T., Y. Rolland, T. Dumont, T. Heymes, C. Authemayou, M. Corsini, and M. Fornari (2009), ^{40}Ar/^{39}Ar dating of Penninic Front tectonic displacement (W Alps) during the lower Oligocene (31–34 Ma), *Terra Nova*, *21*, 127–136, doi:10.1111/j.1365-3121.2009.00865.x.

Teyssier, C., and D. Whitney (2002), Gneiss domes and orogeny, *Geology*, *30*, 1139–1142, doi:10.1130/0091-7613(2002)030<1139:GDAO>2.0. CO;2.

Tirel, C., J.-P. Brun, and E. Burov (2008), Dynamics and structural development of metamorphic core complexes, *J. Geophys. Res.*, *113*, B04403, doi:10.1029/2005JB003694.

Triboulet, C., and C. Audren (1985), Continuous reactions between biotite, garnet, staurolite, kyanite-sillimanite-andalusite and P-T-time-deformation path in mica-schists from the estuary of the river Vilaine, south Brittany, France, *J. Metamorph. Geol.*, *3*, 91–105, doi:10.1111/j.1525-1314.1985.tb00307.x.

Triboulet, C., and C. Audren (1988), Controls on P-T-t-deformation path from amphibole zonation during progressive metamorphism of basic rocks (estuary of the river Vilaine, south Brittany, France), *J. Metamorph. Geol.*, *6*, 117–133, doi:10.1111/j.1525-1314.1988.tb00412.x.

Turrillot, P., R. Augier, and M. Faure (2009), The top-to-the-southeast Sarzeau shear zone and its place in the late-orogenic extensional tectonics of southern Armorica, *Bull. Soc. Geol. Fr.*, *180*, 247–261, doi:10.2113/gssgfbull.180.3.247.

Vanderhaeghe, O. (2004), Structural development of the Naxos migmatite dome, *Spec. Pap. Geol. Soc. Am.*, *380*, 211–226.

Vanderhaeghe, O., and C. Teyssier (2001), Partial melting and flow of orogens, *Tectonophysics*, *342*, 451–472, doi:10.1016/S0040-1951(01)00175-5.

Van der Molen, I., and M. S. Paterson (1979), Experimental deformation of partially melted granite, *Contrib. Mineral. Petrol.*, *70*, 299–318, doi:10.1007/BF00375359.

Vauchez, A., D. Maillet, and J. Sougy (1987), Strain and deformation mechanisms in the Variscan nappes of Vendé, South Brittany, France, *J. Struct. Geol.*, *9*, 31–40, doi:10.1016/0191-8141(87)90041-1.

Vidal, P. (1980), L'évolution polyorogénique du Massif Armoricain: Apport de la géochronologie et de la géochimie isotopique du strontium, *Mem. Soc. Geol. Mineral. Bretagne*, *21*, 162 pp.

Villa, I. M. (1998), Isotopic closure, *Terra Nova*, *10*, 42–47, doi:10.1046/j.1365-3121.1998.00156.x.

Watts, M. S., and G. D. Williams (1979), Faults rocks as indicators of progressive shear deformation in the Guingamp region, Brittany, *J. Struct. Geol.*, *1*, 323–332, doi:10.1016/0191-8141(79)90007-5.

Wernicke, B. (1981), Low-angle normal faults in the Basin and Range Province: Nappe tectonics in an extending orogen, *Nature*, *291*, 645–648, doi:10.1038/291645a0.

Wernicke, B. (1992), Cenozoic extensional tectonics of the U.S. Cordillera, in *The Geology of North America*, vol. G3, *The Cordilleran Orogen: Conterminous U.S.*, edited by B. C. Burchfiel, P. W. Lipman, and M. L. Zoback, pp. 553–581, Geol. Soc. of Am., Boulder, Colo.

R. Augier, M. Faure, and P. Turrillot, Institut des Sciences de la Terre d'Orléans, Université d'Orléans–CNRS UMR 6113–Université François Rabelais–Tours–INSU, F-45071 Orléans CEDEX 2, France. (paul.turrillot@univ-orleans.fr)

P. Monié, UMR 5243, Université de Montpellier 2, CNRS, F-34095 Montpellier 5, France.